



## **Further Studies on Oceanic Biogeochemistry and Carbon Cycling**

*S.R. Signorini*

*C.R. McClain*

## The NASA STI Program Office ... in Profile

Since its founding, NASA has been dedicated to the advancement of aeronautics and space science. The NASA Scientific and Technical Information (STI) Program Office plays a key part in helping NASA maintain this important role.

The NASA STI Program Office is operated by Langley Research Center, the lead center for NASA's scientific and technical information. The NASA STI Program Office provides access to the NASA STI Database, the largest collection of aeronautical and space science STI in the world. The Program Office is also NASA's institutional mechanism for disseminating the results of its research and development activities. These results are published by NASA in the NASA STI Report Series, which includes the following report types:

- **TECHNICAL PUBLICATION.** Reports of completed research or a major significant phase of research that present the results of NASA programs and include extensive data or theoretical analysis. Includes compilations of significant scientific and technical data and information deemed to be of continuing reference value. NASA's counterpart of peer-reviewed formal professional papers but has less stringent limitations on manuscript length and extent of graphic presentations.
- **TECHNICAL MEMORANDUM.** Scientific and technical findings that are preliminary or of specialized interest, e.g., quick release reports, working papers, and bibliographies that contain minimal annotation. Does not contain extensive analysis.
- **CONTRACTOR REPORT.** Scientific and technical findings by NASA-sponsored contractors and grantees.

- **CONFERENCE PUBLICATION.** Collected papers from scientific and technical conferences, symposia, seminars, or other meetings sponsored or cosponsored by NASA.
- **SPECIAL PUBLICATION.** Scientific, technical, or historical information from NASA programs, projects, and mission, often concerned with subjects having substantial public interest.
- **TECHNICAL TRANSLATION.** English-language translations of foreign scientific and technical material pertinent to NASA's mission.

Specialized services that complement the STI Program Office's diverse offerings include creating custom thesauri, building customized databases, organizing and publishing research results . . . even providing videos.

For more information about the NASA STI Program Office, see the following:

- Access the NASA STI Program Home Page at <http://www.sti.nasa.gov/STI-homepage.html>
- E-mail your question via the Internet to [help@sti.nasa.gov](mailto:help@sti.nasa.gov)
- Fax your question to the NASA Access Help Desk at (301) 621-0134
- Telephone the NASA Access Help Desk at (301) 621-0390
- Write to:  
NASA Access Help Desk  
NASA Center for AeroSpace Information  
7121 Standard Drive  
Hanover, MD 21076-1320



## **Further Studies on Oceanic Biogeochemistry and Carbon Cycling**

*S.R. Signorini, SAIC, Beltsville, MD*

*C.R. McClain, Goddard Space Flight Center, Greenbelt, MD*

National Aeronautics and  
Space Administration

**Goddard Space Flight Center**  
Greenbelt, Maryland 20771

---

Available from:

NASA Center for AeroSpace Information  
7121 Standard Drive  
Hanover, MD 21076-1320  
Price Code: A17

National Technical Information Service  
5285 Port Royal Road  
Springfield, VA 22161  
Price Code: A10

## Prologue

This TM consists of two chapters. Chapter I describes the development of a coupled, one-dimensional biogeochemical model using turbulence closure mixed layer dynamics. The model is applied to the Sargasso Sea at the BATS (Bermuda Atlantic Time Series) site and the results are compared with a previous model study in the same region described in NASA/TP-2001-209991.

Chapter II addresses the sensitivity of global sea-air CO<sub>2</sub> flux estimates to wind speed, temperature, and salinity. This is a revision of a previous analysis documented in NASA/TM –2002-211604. Sensitivity analyses of sea-air CO<sub>2</sub> flux to gas transfer algorithms, climatological wind speeds, sea surface temperature (SST) and salinity (SSS) were conducted for the global oceans and selected regional domains. Large uncertainties in the global sea-air flux estimates are identified due to different gas transfer algorithms, and seasonal wind speed, SST and SSS climatologies. The global annual sea-air flux ranges from -0.6 to -2.3 Gt/yr, depending on the combination of gas transfer algorithm and climatological wind speeds used. However, two of the gas transfer algorithms narrow the range of uncertainty for the estimated sea-air flux (-1.1 to -1.4 Gt/yr). There are significant geographical differences in the distribution of oceanic sources and sinks of CO<sub>2</sub> originating from distinct regional patterns of the seasonal *p*CO<sub>2</sub> variability. Different combinations of SST and SSS global fields resulted in changes as large as 16% on the oceans global sea-air flux. This study shows that climatic changes in the global heat balance may significantly affect the global CO<sub>2</sub> flux via changes in SST. This study also highlights the potential impacts of changes in the oceanic hydrologic cycle on CO<sub>2</sub> fluxes, although salinity changes would be regional and could be either positive or negative. SSS changes in regions of high flux could be significant to the global CO<sub>2</sub> flux.

## **Abstract**

This TM consists of two chapters. Chapter I describes the development of a coupled, one-dimensional biogeochemical model using turbulence closure mixed layer (TCMLM) dynamics. The model is applied to the Sargasso Sea at the BATS (Bermuda Atlantic Time Series) site and the results are compared with a previous model study in the same region described in NASA/TP-2001-209991. The use of the TCMLM contributed to some improvements in the model simulation of chlorophyll, PAR, nitrate, phosphate, and oxygen, but most importantly, the current model achieved good agreement with the data with much more realistic background eddy diffusivity. However, off-line calculations of horizontal transport of biogeochemical properties revealed that one-dimensional dynamics can only provide a limited assessment of the nutrient and carbon balances at BATS. Future studies in the BATS region will require comprehensive three-dimensional field studies, combined with three-dimensional eddy resolving numerical experiments, to adequately quantify the impact of the local and remote forcing on ecosystem dynamics and carbon cycling.

Chapter II addresses the sensitivity of global sea-air CO<sub>2</sub> flux estimates to wind speed, temperature, and salinity. Sensitivity analyses of sea-air CO<sub>2</sub> flux to wind speed climatologies, gas transfer algorithms, SSS and SST were conducted for the global oceans and regional domains. Large uncertainties in the global sea-air flux are identified, primarily due to the different gas transfer algorithms used. The sensitivity of the sea-air flux to SST and SSS is similar in magnitude to the effect of using different wind climatologies. Globally, the mean ocean uptake of CO<sub>2</sub> changes by 5 to 16%, depending upon the combination of SST and SSS used.

## Chapter I

### Development of a Coupled, One Dimensional Biogeochemical Model Using Turbulence Closure Mixed Layer Dynamics and Application to the Sargasso Sea (BATS site)

#### I.1. Background

The mixed layer component of an existing one dimensional biogeochemical model [Signorini *et al.*, 2001a; Signorini *et al.*, 2001b], hereafter referred to as ECO1D, was replaced with a turbulence closure mixed layer model [Mellor and Yamada, 1982]. ECO1D has a bulk model of the mixed layer [Garwood, 1977] such that an explicit profile of the vertical eddy diffusivity ( $k_v$ ), required by the biogeochemical conservation equations, cannot be provided by the model. Instead, an ad-hoc analytical fit scaled to surface wind stress, usually an exponential decay function that matches the mixed layer  $k_v$  value with a much smaller background eddy diffusivity, was used to provide values of  $k_v$  at each depth ( $\Delta z=1$  m). The turbulence closure mixed layer model (TCMLM) has a vertical coordinate system that provides parameter values, including  $k_v$ , at each time step and grid point. Also, the surface boundary layer is resolved more accurately by using a stretched vertical coordinate with higher resolution near the surface. Therefore, the coupling between the physical and biogeochemical processes can be achieved in a more robust and accurate manner.

The new model, consisting of the TCMLM coupled to the biogeochemical conservation equations, was rewritten in Fortran 90/95 [Absoft, 1997] for a Linux machine. The following sections describe the details of the model development and its application to the BATS (Bermuda Atlantic Time Series) site.

#### I.2. Mixed Layer Model

The level 2-1/2 version of the Mellor-Yamada turbulent closure scheme was modified to account for solar flux divergence following the method of Simpson and Dickey [1981]. The method was further modified to account for spectral decomposition of the downward radiation. Details of the spectral method are described in the following section. The details of the closure scheme may be found in Mellor and Yamada [1982]; however, a brief description of the model will be included for completeness. Assuming hydrostatic approximation, the mean zonal and meridional momentum equations are

$$\frac{\partial u}{\partial t} - f(v - v_g) = \frac{\partial}{\partial z}(-\overline{u'w'}) - \mu_b \frac{\partial u}{\partial z} - w \frac{\partial u}{\partial z} \quad (1)$$

$$\frac{\partial v}{\partial t} + f(u - u_g) = \frac{\partial}{\partial z}(-\overline{v'w'}) - \mu_b \frac{\partial v}{\partial z} - w \frac{\partial v}{\partial z} \quad (2)$$

where  $u$  and  $v$  are the mean zonal and meridional velocity components,  $u_g$  and  $v_g$  are the corresponding geostrophic velocities,  $-\overline{u'w'}$  and  $-\overline{v'w'}$  are the vertical turbulent Reynold stresses,  $\mu_b$  is the background diffusivity,  $f$  is the Coriolis parameter and  $t$  is time. The last terms on the right side of (1) and (2) are the vertical advection of momentum. The vertical velocity  $w$  is pre-calculated for model forcing (see Section 5 for details).

The heat conservation equation, which includes the divergence of the downward irradiance in spectral form, is given by

$$\rho c_p \frac{\partial T}{\partial t} + \rho c_p \frac{\partial}{\partial z} (\overline{w'T'}) + \mu_b \frac{\partial T}{\partial z} + w \frac{\partial T}{\partial z} + \overline{U}_{\text{clm}} \cdot \nabla T_{\text{clm}} = Q(z) = \frac{\partial I(z)}{\partial z} \quad (3)$$

where  $T$  is the mean temperature and  $c_p$  is the specific heat of seawater. The first term is the local rate of change of heat, the second term is the vertical divergence of turbulent heat flux. The third term is the vertical advection of heat, and the fourth term is the pre-calculated horizontal heat divergence using climatological currents and temperature three-dimensional fields (see Section 5 for details). The right-hand side of (3) is the vertical divergence of the downward irradiance flux. The vertical distribution of downward irradiance is given by

$$I(z) = \int_{\lambda=280}^{3000} I(\lambda, z) = \int_{z=0}^h \int_{\lambda=280}^{3000} I(\lambda, 0) \exp[a(\lambda)z] d\lambda dz \quad (4)$$

where  $I(\lambda, z)$  is the irradiance per unit wavelength for wavelength  $\lambda$  (nm) at depth  $z$ ,  $a(\lambda)$  is the irradiance attenuation coefficient ( $\text{m}^{-1}$ ) for wavelength  $\lambda$ , and  $z$  is the vertical coordinate positive upward with origin at mean sea level.

The salt conservation equation can be written as

$$\frac{\partial S}{\partial t} + \frac{\partial}{\partial z} (\overline{w'S'}) + \mu_b \frac{\partial S}{\partial z} + w \frac{\partial S}{\partial z} + \overline{U}_{\text{clm}} \cdot \nabla S_{\text{clm}} = Q_F \quad (5)$$

where  $S$  is the salinity and  $Q_F$  represents the sources and sinks of freshwater. As in (3), the vertical advection and horizontal divergence of salt are also included. At the surface,  $Q_F(0) = S(0)[E - P]/dz(0)$ ;  $Q_F = 0$  at all other levels below the surface. Therefore, the salinity equation is coupled to atmospheric moisture divergence/convergence via evaporation minus precipitation ( $E - P$ ). The water density,  $\rho(T, S, z)$ , is calculated using an equation of state.

Turbulent kinetic energy (TKE),  $1/2 q^2 = 1/2 (\overline{u'^2} + \overline{v'^2} + \overline{w'^2})$ , and a turbulent length scale  $l$  are computed. The level 2-1/2 version used here includes the diffusion of TKE, which appears to be important for low wind speed situations. The equation for TKE may be written as



$$\frac{1}{2} \frac{\partial q^2}{\partial t} + \frac{1}{2} \frac{\partial (\overline{w'q^2})}{\partial z} = -\overline{u'w'} \frac{\partial u}{\partial z} - \overline{v'w'} \frac{\partial v}{\partial z} - \frac{g}{\rho} \overline{w'\rho'} - D \quad (6)$$

where the first term is the tendency of TKE, the second term is the diffusion of TKE, the first and second terms on the right side of (6) are the shear production, the third term is the buoyancy production and the last term ( $D$ ) is the dissipation.

The problem is closed by invoking hypotheses and assumptions regarding third moment terms [Mellor, 1973]. Required empirical constants are determined from laboratory flow and are not adjusted. The details of the model are rather involved. However, it is possible to reduce the turbulent Reynolds stress and heat flux terms to the following expressions

$$-\overline{u'w'} = ql\tilde{S}_M(R_{yf}) \frac{\partial u}{\partial z} = k_m \frac{\partial u}{\partial z} \quad (7)$$

$$-\overline{v'w'} = ql\tilde{S}_M(R_{yf}) \frac{\partial v}{\partial z} = k_m \frac{\partial v}{\partial z} \quad (8)$$

$$-\overline{w'T'} = \rho c_p ql\tilde{S}_H(R_{yf}) \frac{\partial T}{\partial z} = k_h \frac{\partial T}{\partial z} \quad (9)$$

$\tilde{S}_M$  and  $\tilde{S}_H$  are stability functions;  $k_m$  and  $k_h$  are the eddy viscosity and eddy diffusion coefficients, respectively. The vertical diffusion coefficient for the biogeochemical model is obtained by adding the eddy diffusivity to the background diffusivity ( $k_v = k_h + \mu_b$ ). The background eddy diffusivity (minimum value attained below the surface mixed layer) can be justified as a parameterization of processes not included in the model such as internal waves [Chen and Annan, 2000]. Oceanographic estimates for the background diffusivity are in the range  $10^{-5} - 10^{-4} \text{ m}^2 \text{ s}^{-1}$  [Christian et al., 1997; Moum and Osborn, 1986; Sharples et al., 2001; Siegel and Domaradzki, 1994]. A deep ocean estimate of an upper bound to the eddy coefficient for vertical diffusion is  $10^{-4} \text{ m}^2 \text{ s}^{-1}$  [Moum and Osborn, 1986].

The flux Richardson number, which is simply the ratio of negative turbulent buoyancy production to shear production, is defined as

$$R_{yf} = \frac{\overline{-g\rho'w'\rho'}}{\overline{-u'w'} \frac{\partial u}{\partial z} - \overline{v'w'} \frac{\partial v}{\partial z}} \quad (10)$$

An important feature is the extinction of turbulence ( $\tilde{S}_M = \tilde{S}_H = 0$ ) for  $R_{yf} > 0.21$  [Mellor, 1973].

The numerical scheme uses a two time step implicit algorithm [Richtmyer and Morton, 1967]. The vertical grid spacing is optimized by using a logarithmic distribution, which is ideal for the input of the penetrative component of solar irradiance. For the BATS application, there are 41 levels for a depth of 350 meters with the density of grid points being greatest near the surface. The time step is 30 minutes.

The boundary conditions for the model (in addition to the surface value for  $Q_F$  in (5)) include

1) wind stress  $\tau_{ox}$ ,  $\tau_{oy}$ :

$$\tau_{ox} = \rho q l \tilde{S}_M(R_{if}) \frac{\partial u}{\partial z} \Big|_{z=0} \quad (11)$$

$$\tau_{oy} = \rho q l \tilde{S}_M(R_{if}) \frac{\partial v}{\partial z} \Big|_{z=0} \quad (12)$$

2) Turbulent heat flux  $H$ :

$$H = \rho c_p q l \tilde{S}_H(R_{if}) \frac{\partial T}{\partial z} \Big|_{z=0} \quad (13)$$

The model is initialized with specified temperature, salinity, and horizontal velocity profiles.

### 1.3. Irradiance Model

The total (infrared plus visible) solar radiation is obtained using the Frouin model [Frouin et al., 1989]. This model provides the total radiation and the photosynthetically available radiation (PAR). The infrared ( $I_{IR}$ ) component is obtained by subtracting the PAR component from the total solar radiation. Using a spectral model for PAR [Gregg and Carder, 1990], the spectral PAR component  $I_{PAR}(\lambda)$  can be determined. The infrared component (for mixed layer model only) and the PAR component (mixed layer and biogeochemical model) of the penetrating irradiance are obtained from

$$I_{IR}(z) = I_{IR}(z - \Delta z) \exp[-a_{IR} \Delta z] \quad (14)$$

$$I_{PAR}(\lambda, z) = I(\lambda, z - \Delta z) \exp[-(a_w(\lambda) + a_{ph}(\lambda)) \Delta z] \quad (15)$$

where  $a_{IR}(3.75 \text{ m}^{-1})$  is the attenuation coefficient for infrared radiation, and  $a_w(\lambda)$  and  $a_{ph}(\lambda)$  are the wavelength-dependent light attenuation coefficients for water and

phytoplankton, respectively. The model has two options for the water attenuation coefficients based on *Baker and Smith* [1982] and *Pope and Fry* [1997]. Two options for chlorophyll-dependent attenuation coefficients are available in the model, those from *Morel* [1988] and those from *Dupouy et al.* [1997]. Figure I-1 shows spectra for water absorption and chlorophyll absorption coefficients using the available model options. Another option is the inclusion of the dissolved matter attenuation coefficients,  $a_{dm}(\lambda)$ . The dissolved matter attenuation coefficients are calculated by applying the IOP (inherent optical properties) model of *Garver and Siegel* [1997], which uses water leaving radiances from 6 SeaWiFS bands as input (level 3 binned monthly composites). The IOP model calculates the attenuation coefficient due to dissolved matter for the 443nm wavelength. The attenuation coefficients for other wavelengths are obtained from

$$a_{dm}(\lambda) = a_{dm}(443) \exp[S(\lambda - 443)] \quad (16)$$

where the exponential decay constant,  $S$ , is chosen to be 0.02061.

A correction is applied to the downward irradiance pathway to account for seawater light refraction following Snell's law. After some algebraic manipulations, the correction is applied to  $\Delta z$  as follows

$$\Delta z' = \frac{\Delta z}{\cos \beta} \quad (17)$$

$$\beta = a \sin \left[ \frac{\alpha_z}{n_s} \right] \quad (18)$$

where  $\alpha_z$  is the solar zenith angle, and  $n_s$  is the seawater refraction coefficient which is expressed as a function of salinity and temperature adapted from Table 3.12 of Neumann and Pierson [1966] as

$$n_s = 10^{-6} (285.77 - 15.65T + 197.67S) + 1.333338 \quad (19)$$

#### I.4. Biogeochemical Model

The biogeochemical model is an upgraded version of the *Signorini et al.* [2001a] model, which includes additional conservation equations for diazotrophs and detritus. The addition of diazotrophs and detritus in the model follow the method of *Fennel et al.* [2002]. Figure I-2 shows a diagram illustrating the model components and their couplings. The governing equations for the biogeochemical model are

$$\frac{\partial P}{\partial t} + w \frac{\partial P}{\partial z} - \frac{\partial}{\partial z} \left[ k_v \frac{\partial P}{\partial z} \right] = \mu_{phy} P - \mu_{zoo} Z - R_{phy,NO_3} (P - P_o) - M_{phy,det} (P - P_o) \quad (20)$$

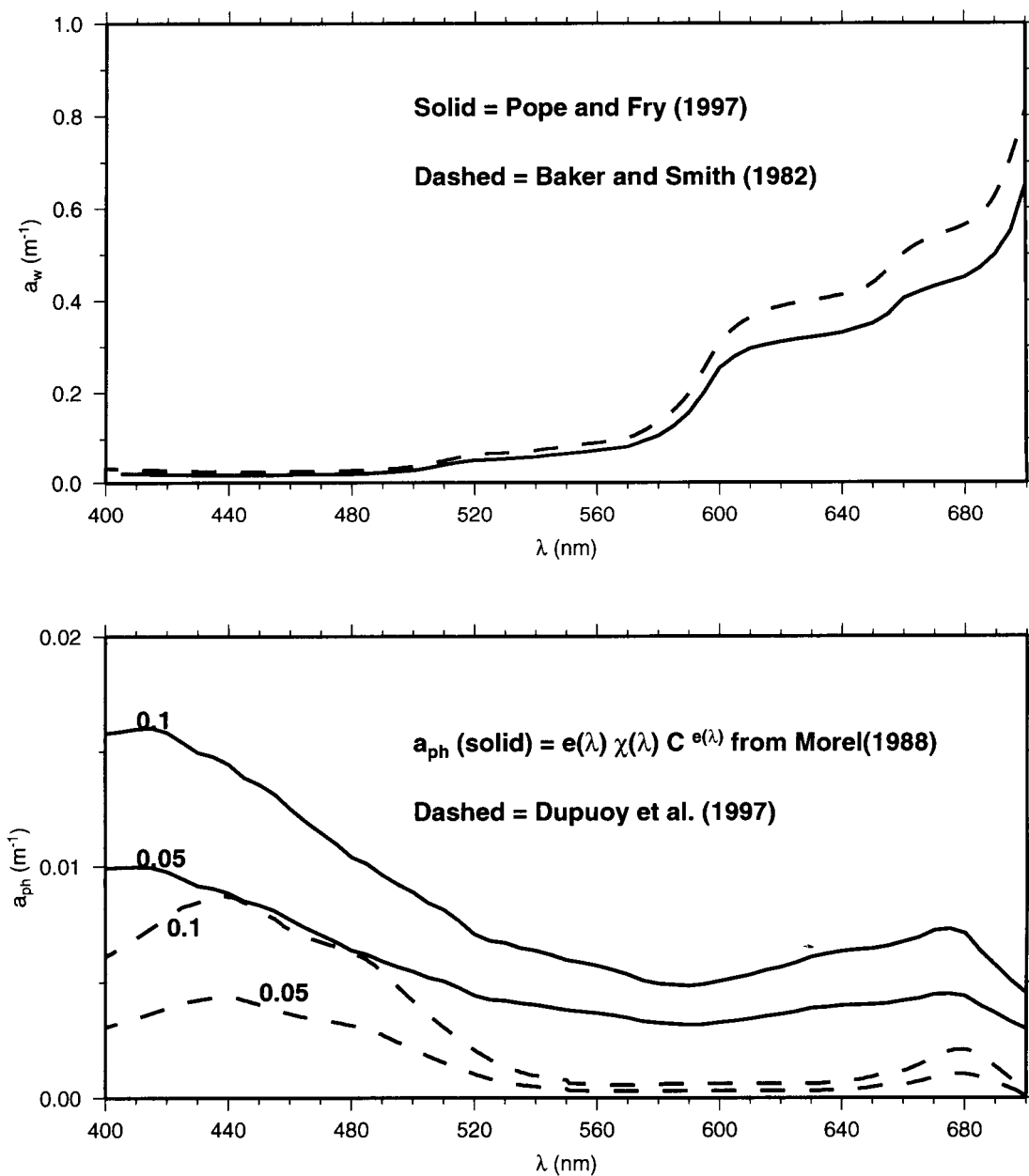


Figure I-1. Spectral absorption coefficients for water ( $a_w$ ) and chlorophyll ( $a_{chl}$ ).

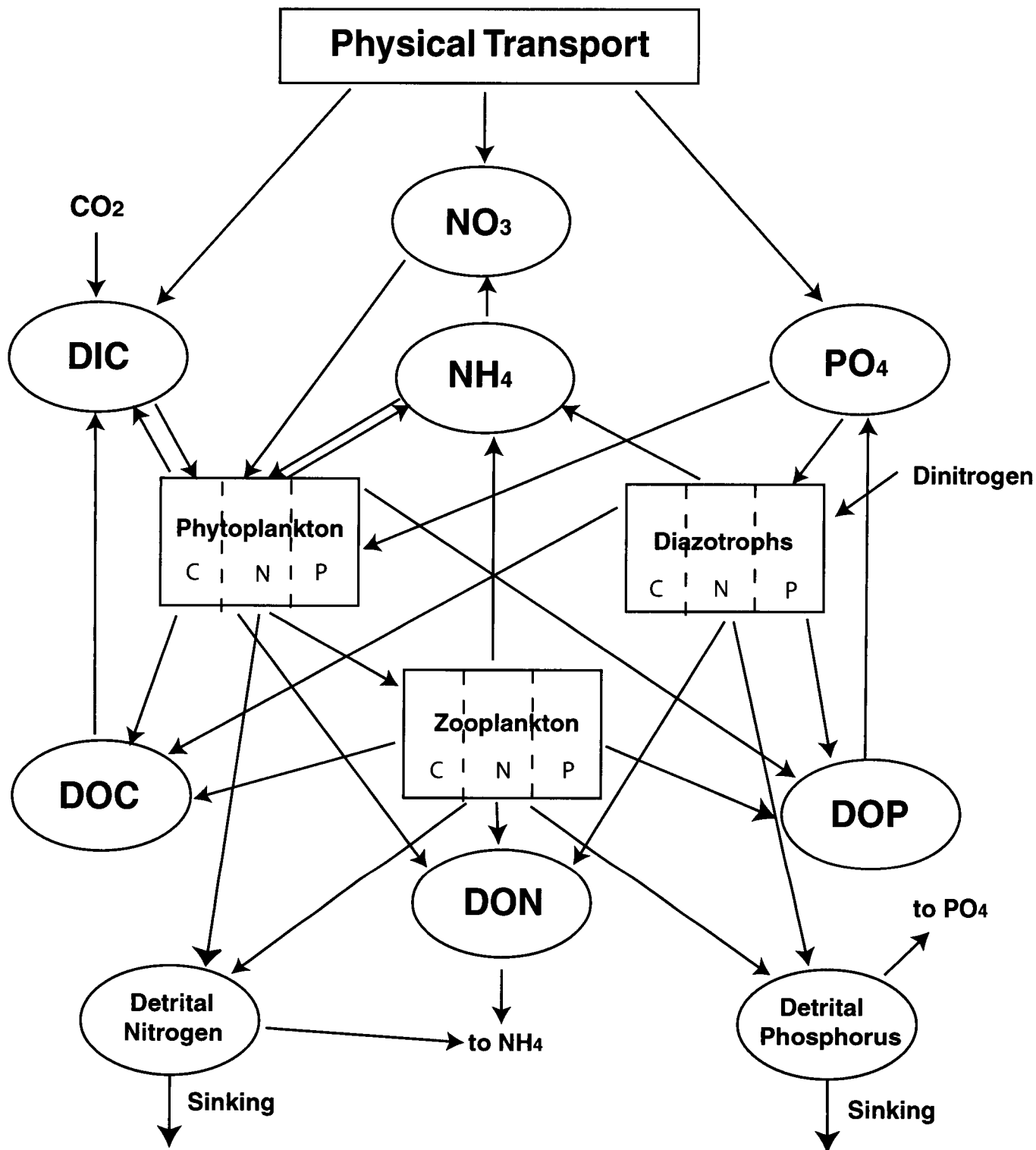


Figure I-2. Flowchart of model components showing the interaction between the nitrogen, phosphorus, and carbon pools.

$$\frac{\partial NF}{\partial t} + w \frac{\partial NF}{\partial z} - \frac{\partial}{\partial z} \left[ k_v \frac{\partial NF}{\partial z} \right] = \mu_{nf} NF - R_{nf,NO_3} NF^2 - M_{nf,det} (NF - NF_o) \quad (21)$$

$$\frac{\partial Z}{\partial t} + w \frac{\partial Z}{\partial z} - \frac{\partial}{\partial z} \left[ k_v \frac{\partial Z}{\partial z} \right] = \gamma \mu_{zoo} Z - E_{zoo,NO_3} (Z - Z_o) - M_{zoo,det} Z^2 \quad (22)$$

$$\begin{aligned} \frac{\partial NH_4}{\partial t} + w \frac{\partial NH_4}{\partial z} - \frac{\partial}{\partial z} \left[ k_v \frac{\partial NH_4}{\partial z} \right] &= a_p M_{phy,det} (P - P_o) + R_{phy,NO_3} (P - P_o) - \pi_1 \mu_{phy} P \\ &+ rem det_N + a_p M_{nf,det} (NF - NF_o) + R_{nf,NO_3} NF^2 + a_z M_{zoo,det} Z^2 \\ &+ E_{zoo,NO_3} (Z - Z_o) - A_n + k_{rn} DON \end{aligned} \quad (23)$$

$$\begin{aligned} \frac{\partial PO_4}{\partial t} + w \frac{\partial PO_4}{\partial z} - \frac{\partial}{\partial z} \left[ k_v \frac{\partial PO_4}{\partial z} \right] + \bar{U}_{clm} \cdot \nabla PO_4^{clm} &= \\ [a_p M_{nf,det} (NF - NF_o) - \mu_{nf} NF] \frac{1}{r_2} & \\ + [(a_p M_{phy,det} + R_{phy,NO_3}) (P - P_o) - \mu_{phy} P + a_z M_{zoo,det} Z^2 + E_{zoo,NO_3} (Z - Z_o)] \frac{1}{r_1} & \\ + k_{rp} DOP + rem det_p & \end{aligned} \quad (24)$$

$$\begin{aligned} \frac{\partial NO_3}{\partial t} + w \frac{\partial NO_3}{\partial z} - \frac{\partial}{\partial z} \left[ k_v \frac{\partial NO_3}{\partial z} \right] + \bar{U}_{clm} \cdot \nabla NO_3^{clm} &= -\pi_2 \mu_{phy} P + A_n + R_{nf,NO_3} NF^2 \\ (25) \end{aligned}$$

$$\begin{aligned} \frac{\partial DOC}{\partial t} + w \frac{\partial DOC}{\partial z} - \frac{\partial}{\partial z} \left[ k_v \frac{\partial DOC}{\partial z} \right] &= \frac{1}{\rho} [0.15 \mu_{phy} P + a_p M_{phy,det} (P - P_o) \\ + a_z M_{zoo,det} Z^2 + 0.05 \mu_{nf} NF + a_p M_{nf,det} (NF - NF_o)] &\left( \frac{C}{N} \right)_{Red} - k_{rc} DOC \end{aligned} \quad (26)$$

$$\begin{aligned} \frac{\partial \text{DON}}{\partial t} + w \frac{\partial \text{DON}}{\partial z} - \frac{\partial}{\partial z} \left[ k_v \frac{\partial \text{DON}}{\partial z} \right] &= a_p' M_{\text{phy,det}} (P - P_o) + a_z' M_{\text{zoo,det}} Z^2 \\ + a_p' M_{\text{nf,det}} (NF - NF_o) - k_{rn} \text{DON} \end{aligned} \quad (27)$$

$$\begin{aligned} \frac{\partial \text{DOP}}{\partial t} + w \frac{\partial \text{DOP}}{\partial z} - \frac{\partial}{\partial z} \left[ k_v \frac{\partial \text{DOP}}{\partial z} \right] &= [a_p' M_{\text{phy,det}} (P - P_o) + a_z' M_{\text{zoo,det}} Z^2] \frac{1}{r_1} \\ + a_p' M_{\text{nf,det}} (NF - NF_o) \frac{1}{r_2} - k_{rp} \text{DOP} \end{aligned} \quad (28)$$

$$\begin{aligned} \frac{\partial \text{det}_N}{\partial t} + w \frac{\partial \text{det}_N}{\partial z} - \frac{\partial}{\partial z} \left[ k_v \frac{\partial \text{det}_N}{\partial z} \right] &= (1 - a_p - a_p') [M_{\text{phy,det}} (P - P_o) \\ + M_{\text{nf,det}} (NF - NF_o)] + (1 - \gamma) \mu_{zoo} Z + (1 - a_z - a_z') M_{\text{zoo,det}} Z^2 \\ - w_{\text{det}} \frac{\partial \text{det}_N}{\partial z} - \text{remdet}_N \end{aligned} \quad (29)$$

$$\begin{aligned} \frac{\partial \text{det}_p}{\partial t} + w \frac{\partial \text{det}_p}{\partial z} - \frac{\partial}{\partial z} \left[ k_v \frac{\partial \text{det}_p}{\partial z} \right] &= (1 - a_p - a_p') [M_{\text{phy,det}} (P - P_o) \frac{1}{r_1} \\ + M_{\text{nf,det}} (NF - NF_o) \frac{1}{r_2}] + [(1 - \gamma) \mu_{zoo} Z + (1 - a_z - a_z') M_{\text{zoo,det}} Z^2] \frac{1}{r_1} \\ - w_{\text{det}} \frac{\partial \text{det}_p}{\partial z} - \text{remdet}_p \end{aligned} \quad (30)$$

$$\begin{aligned} \frac{\partial \text{TCO}_2}{\partial t} + w \frac{\partial \text{TCO}_2}{\partial z} - \frac{\partial}{\partial z} \left[ k_v \frac{\partial \text{TCO}_2}{\partial z} \right] + \bar{U}_{\text{clm}} \cdot \nabla \text{TCO}_2^{\text{clm}} &= \delta(z) \frac{\text{FCO}_2}{\rho} \\ - \frac{N_p}{\rho} \left( \frac{\text{C}}{\text{N}} \right)_{\text{Red}} + \frac{1}{S_o} \frac{\partial S}{\partial t} \text{TCO}_2 \end{aligned} \quad (31)$$

$$\frac{\partial O_2}{\partial t} + w \frac{\partial O_2}{\partial z} - \frac{\partial}{\partial z} \left[ k_v \frac{\partial O_2}{\partial z} \right] = \delta(z) \frac{FO_2}{\rho} + \frac{N_p}{\rho} \left( \frac{O_2}{N} \right)_{\text{Red}} \quad (32)$$

$$N_p = \mu_{\text{phy}} P - (a_p L_{\text{phy},\text{det}} + L_{\text{phy},\text{NO}_3})(P - P_o) - a_z L_{\text{zoo},\text{det}} Z^2 - L_{\text{zoo},\text{NO}_3}(Z - Z_o) \\ - k_{rc} \text{DOC} \left( \frac{N}{C} \right)_{\text{Red}} + \mu_{\text{nf}} NF - a_p L_{\text{nf},\text{det}}(NF - NF_o) - L_{\text{nf},\text{NO}_3} NF^2 - \text{remdet}_N \quad (33)$$

$$\mu_{\text{phy}}(\text{NO}_3, \text{PO}_4, E) = F_{\text{phy}}(E) \min \left[ N_{\text{lim}}, \frac{\text{PO}_4}{k_{\text{Pl}} + \text{PO}_4} \right] \quad (34)$$

$$\mu_{\text{zoo}}(P) = \mu_{\text{zoo}}^{\max} \frac{P^2}{k_{\text{phy}} + P^2} \quad (35)$$

$$N_{\text{lim}} = \text{NH}_{4\text{lim}} + \text{NO}_{3\text{lim}} \quad (36)$$

$$\text{NO}_{3\text{lim}} = \frac{\text{NO}_3}{(K_{\text{NO}_3} + \text{NO}_3)} \frac{(1 - \text{NH}_4)}{(K_{\text{NH}_4} + \text{NH}_4)} \quad (37)$$

$$\text{NH}_{4\text{lim}} = \frac{\text{NH}_4}{(K_{\text{NH}_4} + \text{NH}_4)} \quad (38)$$

$$\pi_1 = \frac{\text{NH}_{4\text{lim}}}{\text{NH}_{4\text{lim}} + \text{NO}_{3\text{lim}}} \quad (39)$$

$$\pi_2 = \frac{\text{NO}_{3\text{lim}}}{\text{NH}_{4\text{lim}} + \text{NO}_{3\text{lim}}} \quad (40)$$



$$F_{\text{phy}}(E) = \frac{\mu_{\text{phy}}^{\max} \alpha_1 E}{\sqrt{(\mu_{\text{phy}}^{\max})^2 + (\alpha_1 E)^2}} \quad (41)$$

$$\mu_{\text{nf}}(\text{PO}_4, E, T, |\tau|) = F_{\text{nf}}(E) \frac{\text{PO}_4}{k_{\text{p2}} + \text{PO}_4} \text{ampl}(T, |\tau|) \quad (42)$$

$$F_{\text{nf}}(E) = \frac{\mu_{\text{nf}}^{\max} \alpha_2 E}{\sqrt{(\mu_{\text{nf}}^{\max})^2 + (\alpha_2 E)^2}} \quad (43)$$

$$\text{ampl}(T, |\tau|) = \begin{cases} \frac{1}{3}[\tanh(2(T-T_{\text{crit}}))+1]+\frac{1}{3} & \text{if } |\tau| \leq \tau_{\text{crit}} \\ \frac{1}{6}[\tanh(2(T-T_{\text{crit}}))+1]+\frac{1}{6} & \text{if } |\tau| > \tau_{\text{crit}} \end{cases} \quad (44)$$

$r_2=45$  is N:P for nitrogen fixers

$r_1=14$  is N:P for other phytoplankton

$$PP = (\mu_{\text{phy}} P + \mu_{\text{nf}} NF) \left( \frac{C}{N} \right)_{\text{Red}} C_{\text{MW}} \quad (45)$$

$$\left( \frac{C}{N} \right)_{\text{Red}} = 6.625 \quad C_{\text{MW}} = 12$$

$$\text{Chl} - a = \text{Chl:N}(P + NF) \quad (46)$$

$$\text{Chl:N} = \text{Chl:N}^{\max} - (\text{Chl:N}^{\max} - \text{Chl:N}^{\min}) \frac{I_{\text{PAR}}}{I_*} \quad I_{\text{PAR}} < I_* \quad (47)$$

$$\text{Chl:N} = \text{Chl:N}^{\min} \quad I_{\text{PAR}} \geq I_*$$

$$\text{Chl:N}^{\min} = 0.8 \text{ mg chl-a (mmol N)}^{-1}$$

$$\text{Chl:N}^{\max} = 1.6 \text{ mg chl-a (mmol N)}^{-1}$$

The subscripts phy, zoo, nf, det, and clm refer to phytoplankton, zooplankton, nitrogen fixers, detritus, and climatology, respectively. Table I-1 defines the model state variables and Table I-2 provides the definition of the model parameters and values used.

**Table I-1. Model state variables.**

Symbol	Unit	Variable	Background value
NO <sub>3</sub>	mmol N m <sup>-3</sup>	Dissolved inorganic nitrogen	
PO <sub>4</sub>	mmol P m <sup>-3</sup>	Dissolved inorganic phosphorus	
NH <sub>4</sub>	mmol N m <sup>-3</sup>	Ammonium	
O <sub>2</sub>	μmol kg <sup>-1</sup>	Dissolved oxygen	
TCO <sub>2</sub>	μmol kg <sup>-1</sup>	Dissolved inorganic carbon	
NF	mmol N m <sup>-3</sup>	Nitrogen-fixing phytoplankton	NF <sub>0</sub> =0.001
P	mmol N m <sup>-3</sup>	Other phytoplankton	
Z	mmol N m <sup>-3</sup>	Zooplankton	
DON	mmol N m <sup>-3</sup>	Dissolved organic nitrogen	
DOP	mmol P m <sup>-3</sup>	Dissolved organic phosphorus	
DOC	μmol kg <sup>-1</sup>	Dissolved organic carbon	
det <sub>N</sub>	mmol N m <sup>-3</sup>	Detrital particulate nitrogen	
det <sub>P</sub>	mmol P m <sup>-3</sup>	Detrital particulate phosphate	

## I.5. Application to the BATS site

The model was applied to the Bermuda Atlantic Time Series (BATS) site and the results compared with a previous version of the biogeochemical model [Signorini *et al.*, 2001a] with off-line physical forcing (temperature, salinity, and mixed layer depth) derived from CTD casts. The major additions and modifications to the current model are

- The physical forcing parameters, temperature, salinity, mixed layer depth, and vertical eddy diffusivity, are now computed using the TCMLM
- The Ekman pumping velocity was derived from daily NCEP winds. The previous model used Ekman pumping velocity derived from monthly winds.
- The horizontal divergence of heat, salt, nitrate, phosphate are estimated from seasonal climatology of currents (geostrophic plus Ekman drift), nitrate, and phosphate (see Figure I-4)
- The horizontal divergence of dissolved inorganic carbon (DIC) is estimated from seasonal climatology of currents and the DIC algorithm of Lee *et al.*, which is dependent on temperature, salinity, apparent oxygen utilization (AOU), and silicate, also obtained from seasonal climatology (see Figure I-4).
- A dilution term (salinity-dependent) was introduced for the DIC conservation equation (31)

**Table I-2. Model Parameters.**

Symbol	Value	Unit	Parameter
$R_{\text{phy},\text{NO}_3}$	0.05	$\text{d}^{-1}$	Phytoplankton respiration rate
$M_{\text{phy},\text{det}}$	0.05	$\text{d}^{-1}$	Phytoplankton mortality rate
$k_{\text{NO}_3}$	0.025	$\text{mmol N m}^{-3}$	Half-saturation concentration for $\text{NO}_3$ uptake
$k_{\text{NH}_4}$	0.025	$\text{mmol N m}^{-3}$	Half-saturation concentration for $\text{NH}_4$ uptake
$k_{\text{P}_1}$	0.0025	$\text{mmol P m}^{-3}$	Half-saturation concentration for $\text{PO}_4$ uptake
$r_1$	14	$\text{mmol N: mmol P}$	Stoichiometry of phytoplankton and zooplankton
$\mu_{\text{phy}}^{\text{max}}$	3.0	$\text{d}^{-1}$	Maximum growth rate of phytoplankton
$\alpha_1$	0.25	$(\text{W m}^{-2})^{-1} \text{d}^{-1}$	Initial P-I slope of phytoplankton
$R_{\text{nf},\text{NO}_3}$	0.17	$\text{d}^{-1}(\text{mmol N m}^{-3})^{-1}$	Diazotrophic respiration rate
$M_{\text{nf},\text{det}}$	0.05	$\text{d}^{-1}$	Diazotrophic mortality rate
$\mu_{\text{nf}}^{\text{max}}$	0.3	$\text{d}^{-1}$	Maximum growth rate of diazotrophs
$k_{\text{P}_2}$	0.00001	$\text{mmol P m}^{-3}$	Half-saturation concentration for $\text{PO}_4$ uptake by diazotrophs
$\alpha_2$	0.01	$(\text{W m}^{-2})^{-1} \text{d}^{-1}$	Initial P-I slope of diazotrophs
$T_{\text{crit}}$	24.75	$^{\circ}\text{C}$	Critical temperature for diazotroph growth
$\tau_{\text{crit}}$	0.062	$\text{N m}^{-2}$	Critical wind stress for diazotroph growth
$r_2$	45	$\text{mmol N: mmol P}$	Stoichiometry of diazotrophs
$\mu_{\text{zoo}}^{\text{max}}$	1.0	$\text{d}^{-1}$	Maximum grazing rate of zooplankton
$k_{\text{phy}}$	0.25	$(\text{mmol N m}^{-3})^{-2}$	Half-saturation concentration for ingestion by zooplankton
$\gamma$	0.75	Dimensionless	Zooplankton assimilation efficiency
$E_{\text{zoo},\text{NO}_3}$	0.05	$\text{d}^{-1}$	Zooplankton excretion rate
$M_{\text{zoo},\text{det}}$	0.05	$\text{d}^{-1}(\text{mmol N m}^{-3})^{-1}$	Zooplankton mortality rate
$rem$	0.001	$\text{d}^{-1}$	Remineralization rate of detritus
$w_{\text{det}}$	2.5	$\text{m d}^{-1}$	Sinking velocity of detritus
$k_{\text{m}}$	0.00001	$\text{d}^{-1}$	Remineralization rate of DON
$k_{\text{rp}}$	0.00001	$\text{d}^{-1}$	Remineralization rate of DOP
$k_{\text{rc}}$	0.0005	$\text{d}^{-1}$	Remineralization rate of DOC
$a_p$	0.8	Dimensionless	Fraction of dead phytoplankton converted to ammonium
$a_z$	0.8	Dimensionless	Fraction of dead zooplankton converted to ammonium
$a_p'$	0.1	Dimensionless	Fraction of dead phytoplankton converted to DOM
$a_z'$	0.1	Dimensionless	Fraction of dead zooplankton converted to DOM
$A_n^{\text{max}}$	2.0	$\text{mmol N d}^{-1}$	Maximum rate of ammonium nitrification
$D_{\text{min}}$	0.0095	$\text{W m}^{-2}$	Maximum light inhibition dosage for nitrification
$K_D$	0.8	$\text{W m}^{-2}$	Half-saturation light dosage for nitrification photoinhibition

- A correction for light penetration refraction was added based on Snell's law.
- The chlorophyll-dependent  $a_{ph}^*(\lambda)$  from Morel [1988] was added as an option. This option was used in the current simulation.
- An option for light absorption by dissolved matter derived from an IOP model and SeaWiFS water leaving radiances was developed (not used in current simulation).
- Values for DIC and O<sub>2</sub> at the bottom boundary are no longer constant; they were derived off-line from the BATS data time series. The NO<sub>3</sub> and PO<sub>4</sub> bottom boundary values are also obtained similarly, as in the previous model simulation.
- New equations were added to the biogeochemical model for determining the concentrations of diazotrophs, and detritus (nitrogen and phosphorus components).

The following subsections describe the model configuration, forcing, validation, and comparison of results with the previous model.

#### *Data Sources and Model Forcing*

The ecosystem model is physically forced by temperature, salinity, and mixed layer depth from the TCMLM. The BATS biogeochemical data were used for model forcing and validation. The data are discussed in several publications [Bates *et al.*, 1996; Michaels and Knap, 1996; Michaels *et al.*, 1994]. The observed PAR profiles for validation were obtained from the Bermuda Bio-Optics Program (BBOP) database. The 1994-1996 seawater and atmospheric pCO<sub>2</sub> data originate from the carbon dioxide measurements obtained from the R/V Weatherbird II in the Sargasso Sea [Bates *et al.*, 1998]. Most of these data sets were obtained interactively via the web-based data extractor maintained by BBSR (Bermuda Biological Station for Research, Inc.; [www.bbsr.edu/cintoo/bats/bats.html](http://www.bbsr.edu/cintoo/bats/bats.html)). The eddy-induced vertical velocity time series was calculated (see Section 3) from the merged TOPEX/Poseidon-European Remote Sensing Satellite (ERS), 1/3°, 7-day sea-surface height anomaly (SSHA) grids [AVISO, 1997]. The SSHA data were obtained via anonymous ftp from the AVISO data distribution server (<ftp://ftp.cls.fr/pub/oceano/AVISO>). Three-hourly wind speed data for the gas transfer formulation, and for mixed layer model forcing, were obtained from the Bermuda Airport weather station. The gridded winds to calculate the Ekman pumping vertical velocity, and cloud cover data to calculate surface PAR, and meteorological parameters (precipitation, air temperature, and humidity) to calculate surface heat and freshwater fluxes for the TCMLM, were obtained from the NCEP/NCAR Reanalysis Project [Kalnay *et al.*, 1996] daily products.

The BATS region is characterized by energetic mesoscale eddies that provide vertical transport of nutrients to the euphotic zone via eddy pumping [McGillicuddy *et al.*, 1999; McGillicuddy *et al.*, 1998a; Siegel *et al.*, 1999]. The vertical velocity variability in the

BATS study area is affected primarily by vertical displacements of the thermocline imparted by the migration of mesoscale eddies through the area [McGillicuddy *et al.*, 1998b; Siegel *et al.*, 1999]. This eddy pumping mechanism has been demonstrated to have a significant impact on the nutrient budget at BATS [Siegel *et al.*, 1999]. However, Oeschlies [2002], using a three-dimensional eddy-resolving ( $1/9^\circ$  resolution) model, concluded that eddy pumping has a much more limited role in nitrate supply at BATS than reported by previous studies. We obtained the eddy pumping vertical velocity ( $w_{eddy}$ ) time series for the BATS location by taking the first derivative of the SSHA and scaling it to the pycnocline displacement using the scale factor of 4 meters of thermocline displacement for each cm of SSHA. The scale factor originates from Siegel *et al.* [1999].

Figure I-3 shows time series of geostrophic currents, SSHA, and vertical velocity for the available time period of 21 October 1992 through 13 February 2002. An uninterrupted time series of eddy vertical velocity, covering the period of 1990-1998, was constructed by filling the missing points (1 January 1990 – 20 October 1992) with data from adjacent years. The model was run for the period 1 January 1990 – 31 December 1998, but the first two years of simulation were discarded as they served as spin-up years. The vertical velocity profile,  $w(z)$ , is parameterized as,

$$\begin{aligned} w(z) &= w_{eddy} \frac{z}{200}, \quad \text{for } z \leq 200m \\ w(z) &= w_{eddy}, \quad \text{for } 200m < z \leq 350m \end{aligned} \tag{48}$$

The 200 m transition depth follows the [Siegel *et al.*, 1999] empirical parameterization. Below 200 meters isopycnal displacements are related to SSHA as a 4-m isopleth displacement for each 1-cm of sea level height anomaly, while above 200 meters the displacement is modeled as a decreasing linear profile that extrapolates to zero at the sea surface. The weekly eddy-induced vertical velocity ranges from  $-5.3$  to  $+5.9 \text{ m d}^{-1}$  (solid line), while the daily Ekman pumping ranges from  $-0.95$  to  $+0.62 \text{ m d}^{-1}$  (dotted line). The two components of the vertical velocity were added to force the model. The kinematic approach for eddy pumping derived by Siegel *et al.* [1999] requires the determination of a minimum SLA for a given uplifting event and assumes that all the nitrate brought to the euphotic zone is instantaneously used by phytoplankton. To meet these requirements, the eddy pumping events to force the model are obtained by specifying thresholds for SLA and  $w$ . The eddy pumping events are “turned on” whenever the SLA is negative (pycnocline uplifting) and the vertical velocity is positive. As an option, the thresholds for SLA and  $w$  can be turned off in the model allowing for upwelling (positive  $w$ ) and downwelling (negative  $w$ ) events to occur with no constraints. A comparison of the two methods will be offered in the forthcoming section discussing sensitivity tests.

The geostrophic velocity components used in the TCMLM momentum equations are pre-calculated using the thermal wind equations at grid points surrounding the BATS site. The vertical profiles of geostrophic velocity are obtained from a combination of

### TP/ERS-Derived Geostrophic Current, MSLA, and $w$ at BATS

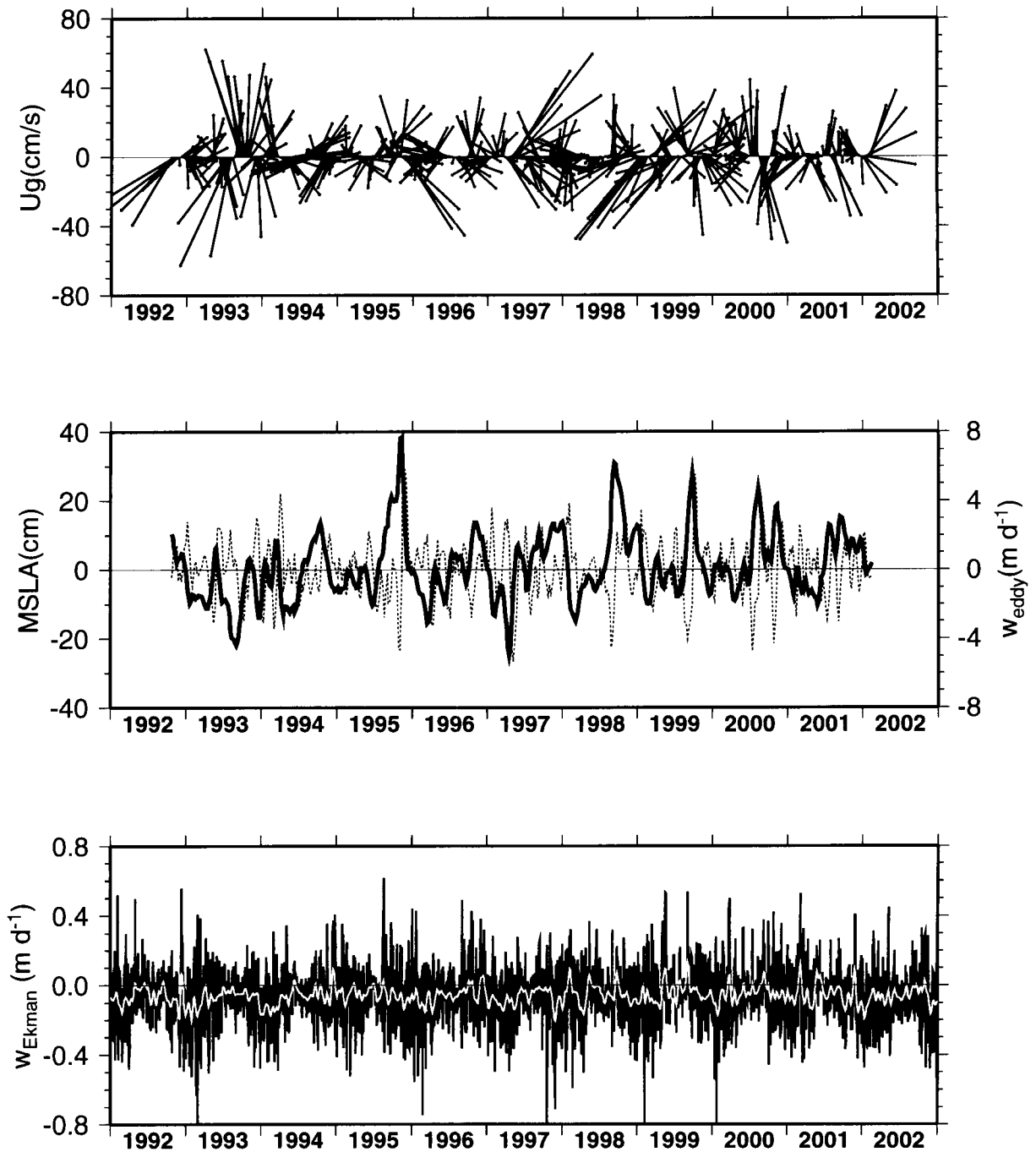


Figure I-3. Time series of geostrophic currents (top), mean sea level anomaly and eddy pumping velocity (middle), and Ekman vertical velocity (bottom). The white line in the bottom tier is the low-pass-filtered Ekman velocity.

hydrographic data [Conkright *et al.*, 1998] from seasonal climatologies (baroclinic component) and SSHA (barotropic eddy component). The horizontal divergence of  $T$ ,  $S$ ,  $\text{NO}_3$ ,  $\text{PO}_4$ , and  $\text{TCO}_2$  (Figure I-4) were calculated off-line using seasonal climatological data. When applied to the model, the horizontal divergence of  $\text{PO}_4$  derived from the seasonal climatology caused large discrepancies between the model and observed  $\text{PO}_4$  profiles. The cause of these discrepancies is not clear. An alternate solution was adopted by obtaining a phosphate versus nitrate linear regression using the BATS data. Nitrate and phosphate are strongly correlated at BATS ( $r^2=0.96$ ) given by

$$\text{PO}_4 = 0.025449 + 0.052924\text{NO}_3 \quad (49)$$

The seasonal profiles of  $\text{TCO}_2$  were obtained using the method of [Lee *et al.*, 1997]. Specifically,

$$\text{TCO}_2 = 1818 + 8.95S - 2.33T - 0.514\text{AOU} + 0.54\text{SiO}_2 \quad (50)$$

where  $T$ ,  $S$ ,  $\text{AOU}$  and  $\text{SiO}_2$  are the World Ocean Atlas 1994 seasonal temperature ( $T$ ), salinity ( $S$ ), apparent oxygen utilization ( $\text{AOU}$ ), and silicate ( $\text{SiO}_2$ ). Data from the World Ocean Atlas 1994 were used instead of the World Ocean Atlas 1998 because the latter data set does not include  $\text{AOU}$ . To calculate the net horizontal divergence, the sum of  $(u\partial C/\partial x + v\partial C/\partial y)$ , where  $C$  represents the variables  $T$ ,  $S$ ,  $\text{NO}_3$ ,  $\text{PO}_4$ , was computed on a  $2\times 2$ -degree grid surrounding the BATS site. The seasonal horizontal velocity components ( $u$ ,  $v$ , profiles) were obtained from the sum of geostrophic component (from hydrographic data) and Ekman drift derived from climatological wind stress components [Oberhuber, 1988] and Ekman dynamics.

The seasonal profiles of PAR, eddy diffusivity, vertical velocity, and  $u$  (east) and  $v$  (north) components of the velocity are shown in Figure I-5. Except for  $u$  and  $v$ , the parameters shown in Figure I-5 are used to force the biogeochemical model.

### *Sensitivity Tests*

The model was run for the period 1990-1998, with the first two years of simulation discarded as spin-up years. The period of 1992-1998 was chosen because it corresponds to the period when most of the observed biogeochemical parameters are concurrently available at BATS. Numerous sensitivity tests were performed with the mixed layer and biogeochemical models to choose the best set of forcing approaches and parameter values that optimize model performance. Table I-3 summarizes the major results. One of the key findings was the model's inability to provide deep enough convective mixing during winter-spring to provide the required supply of nutrients to the euphotic zone. This model deficiency was concluded from five different runs that highlight the effect of vertical mixing on nutrient supply and primary production. The five runs are configured as follows. In run 1 the eddy diffusivity profile generated by the TCMLM is interpolated at the 1-meter grid resolution and applied to the ecosystem model. The nitrate and phosphate profiles are computed prognostically without any constraints. The

**Table I-3.** Summary of major model parameter sensitivity tests and outcomes.

Parameters	Sensitivity	Comments
Number of layers for the stretched vertical coordinate of the mixed layer model.	The winter mixed layer depth, and therefore SST, is very sensitive to the number of layers used.	This sensitivity remains illusive. The best SST values were obtained with 40 layers, which were hardwired in the original MLM code. The use of uniform layer spacing generates instabilities. The model requires a log distribution of grid points near the surface to resolve the air-sea boundary.
Pre-calculated horizontal divergence of nitrate and phosphate from seasonal climatology.	The resulting nitrate and phosphate profiles showed unrealistic behavior. Large nutrient influx in summer causes the spring bloom to shift to summer-fall.	The horizontal divergence terms were turned off.
Eddy pumping.	Primary production is very sensitive to eddy pumping. Two approaches were used for $w$ , eddy upwelling only ( <i>Siegel et al.</i> , 1999) and unconstrained $w$ (+/- values admitted). The two approaches bracket the ideal eddy pumping effect.	A revised approach was implemented following <i>Siegel et al.</i> (1999). The eddy pumping velocity is applied for uplifting events only ( $SLA < 0$ and $w > 0$ ).
Vertical eddy diffusivity	The shape of the nutrient profiles and primary production are sensitive to this mixing parameter.	Typical values for vertical eddy diffusivity are of order of $10^{-5} \text{ m}^2/\text{s}$ ( <i>Gregg</i> , 1987; <i>Ledwell</i> , 1993). An upper bound of $10^{-4} \text{ m}^2 \text{ s}^{-1}$ is given by <i>Munk</i> (1966). A value of $5 \times 10^{-5} \text{ m}^2 \text{ s}^{-1}$ was chosen.
Sea surface salinity.	Most influential on the surface alkalinity and, therefore, an accurate estimate of surface $\text{TCO}_2$ .	Surface salinity was strongly relaxed (order of 1 hour relaxation time scale) to the observed values.
$\text{TCO}_2$ dilution.	A function of salinity changes.	The mean dilution effect on carbon flux is about 1/3 of the sea-air flux.
Half saturation coefficients for nitrate and phosphate uptake.	The magnitude and ratio of these two parameters determines the phytoplankton growth and the stability of nitrate and phosphate concentrations in the euphotic zone.	The value for the half saturation coefficient for nitrate uptake is the same used in the previous model. The corresponding value for phosphate was reduced to 1/10 of its original value to enable a stable nitrate concentration and reasonable growth.
Nitrogen Fixation	The diazotroph growth is modeled as a function of phosphate concentration, light, sea-surface roughness (i.e., wind stress), and temperature ( <i>Fennel et al.</i> , 2002).	Parameter values for diazotroph equation 21 are shown in Table I.2. The predicted 1992-1998 annual average input to new production by $\text{N}_2$ fixation is $0.0035 \text{ mol N/m}^2/\text{yr}$ . This value is close to the $0.004 \text{ mol N/m}^2/\text{yr}$ reported by <i>Orcutt et al.</i> [2001] at BATS.



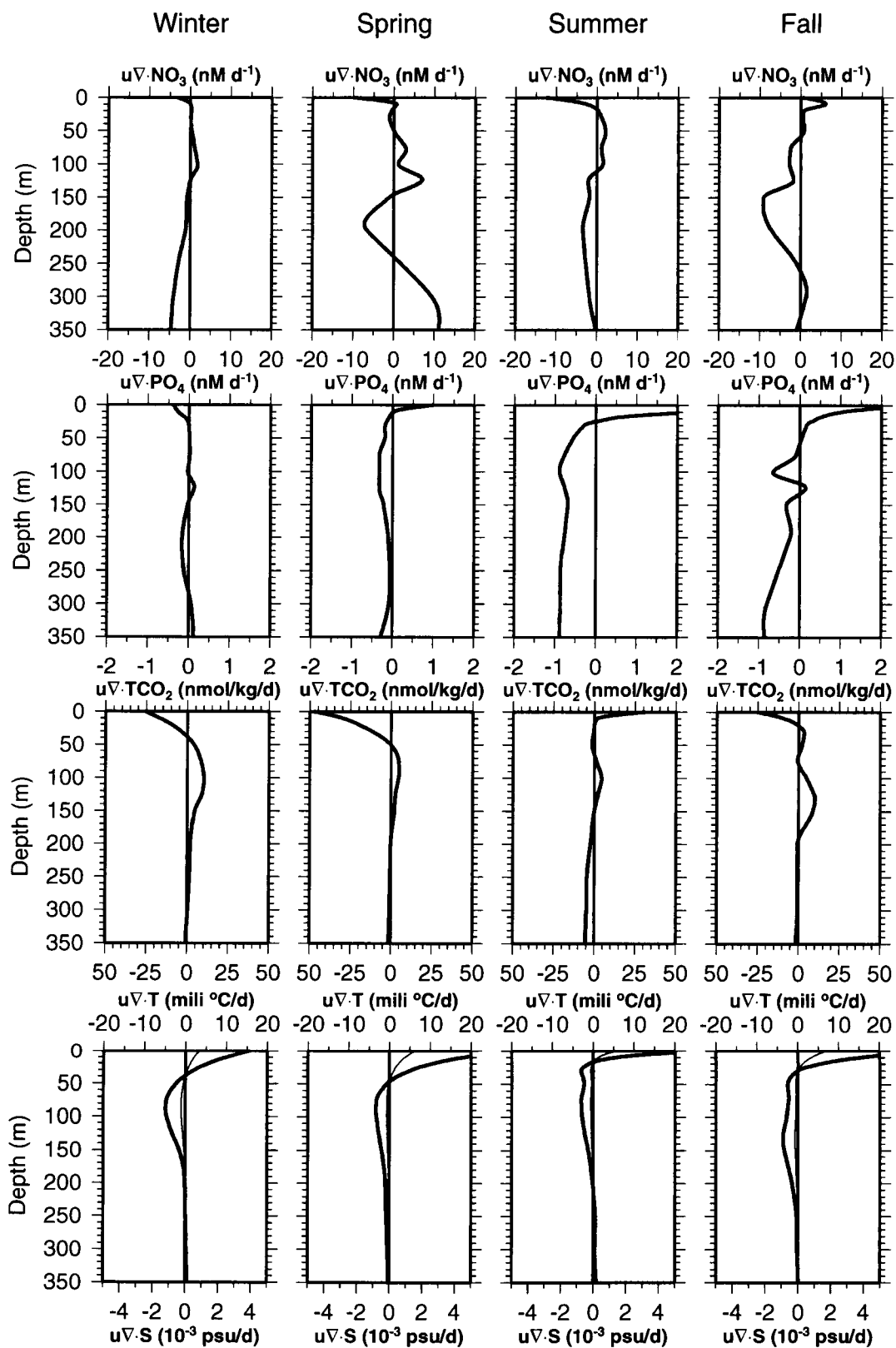


Figure I-4. Seasonal profiles of nitrate, phosphate, dissolved inorganic carbon, temperature, and salinity horizontal divergences derived from seasonal climatologies of currents, nutrients, carbon, and hydrography.

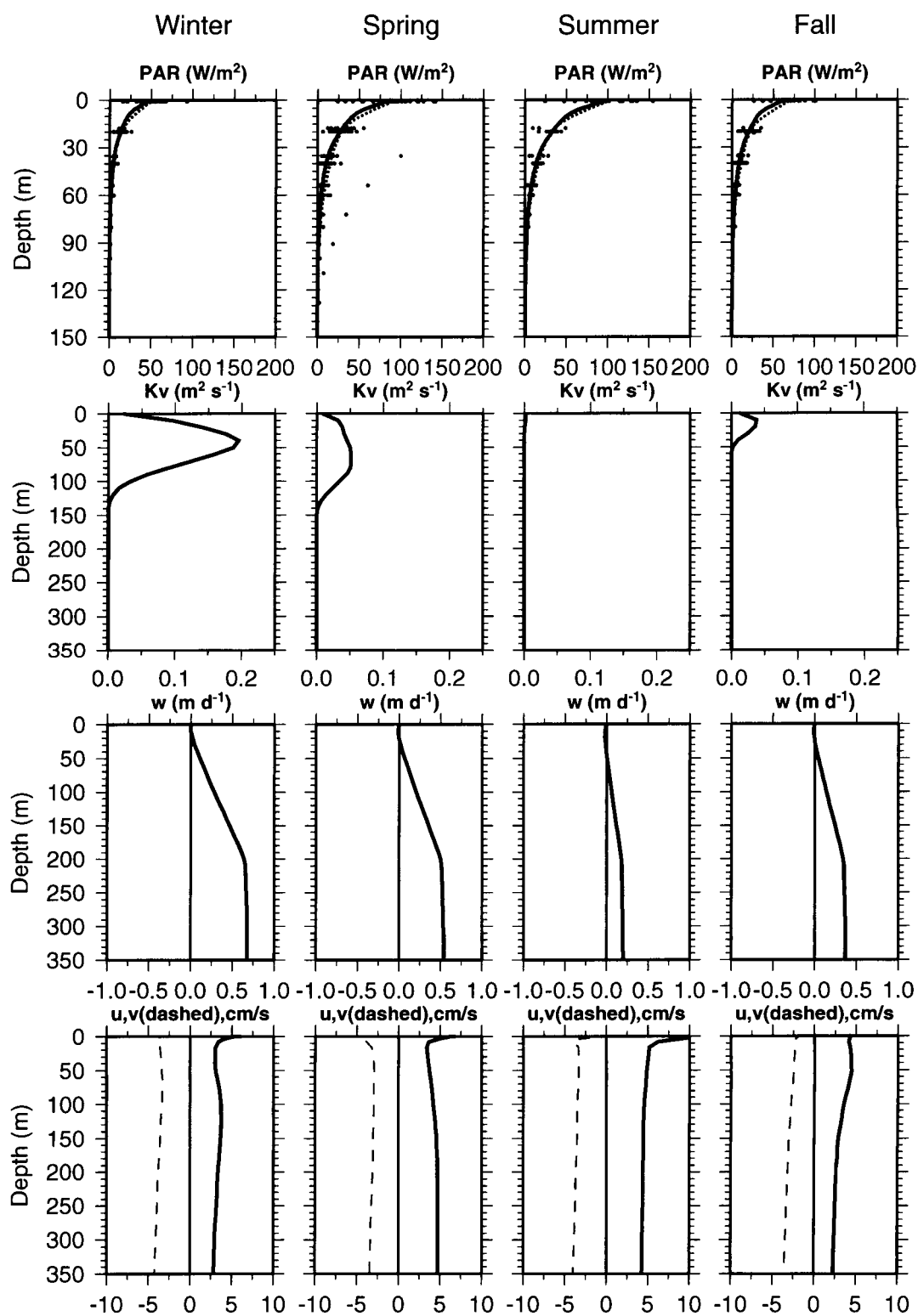


Figure I-5. Seasonal profiles of PAR, vertical eddy diffusion, vertical velocity, and u (solid) and v (dashed) components of horizontal velocity. The black dots superimposed on the PAR profiles are the data points, with the dashed line representing the mean profiles obtained from seasonal averages of the data.

eddy-induced vertical velocity is also free of constraints (upwelling/downwelling mode). Run 2 is similar to run 1, except that the eddy-upwelling mode is enabled (upwelling only, following *Siegel et al.* [1999]) and maintained for the other two subsequent runs. Run 3 is similar to run 2, except that the nitrate and phosphate concentrations below 100m are relaxed to their mean climatological values with a relaxation time scale of 1 month. Run 4 is configured with the nutrient relaxation to climatology and an ad-hoc reconfiguration of the eddy diffusivity profile. The eddy diffusivity profile is reconfigured as follows. First, the mixed layer depth ( $D_{mld}$ ) was calculated by finding the first depth where  $\sigma_\theta(D_{mld}) - \sigma_\theta(0) = \alpha_T \Delta T$ ;  $\alpha_T$  is the coefficient of thermal expansion at sea surface conditions and  $\Delta T$  is chosen to be  $0.5^\circ\text{C}$  [*Siegel et al.*, 1995]. The potential density ( $\sigma_\theta$ ) is obtained from the temperature and salinity profiles generated by the TCMLM. This criterion yields mixed layer depths in winter-spring that are  $\sim 50\text{m}$  deeper than those provided by the criterion used in the TCMLM code, which is based on finding the first depth where  $T(D_{mld}) - T(0) = 0.2^\circ\text{C}$ . The original TCMLM eddy diffusivity profile has a local maximum within the mixed layer, being zero at the surface and the background value below the mixed layer (Figure I-5). The reconfigured eddy diffusivity profile assumes a constant value within the mixed layer equal to the maximum value provided by the TCMLM, similar to the profile assumed in *McClain et al.* [1996]. The background diffusivity is not changed from its original value. A 50-point (50m) running boxcar filter is applied to the profiles for smoothing the transition between the mixed layer and the background values. Finally, run 5 was forced with TCMLM eddy diffusivity, upwelling/downwelling mode, and nutrient relaxation to climatology.

Figures I-6 through I-9 show the seasonal profiles of primary production, chlorophyll, nitrate, and phosphate concentrations obtained from runs 1, 2, 3, and 4 respectively. The seasonal profiles from run 5 are not shown because the profiles are very similar to those from run 3. However, more quantitative results of all five runs will be discussed later in this section. The solid lines are the model profiles while the dashed lines are the seasonal means derived from the data (black dots). Figure I-6 shows the profiles from run 1. The agreement with the data is poor because the net vertical nutrient fluxes into the euphotic zone are too low to maintain the biological demand. It is concluded that the altimeter-derived vertical velocity time series provides too much downwelling and therefore does not promote the required vertical nutrient flux. Figure I-7 shows the profiles from run 2, which was configured with the eddy-upwelling only scheme turned on. Figure I-7 shows an overall agreement with the data, with the exception of the summer-fall primary production which is underestimated by the model, and a much sharper nutricline when compared to the observed nitrate and phosphate profiles. The summer-fall primary production is under-predicted by the model because the surface phosphate concentration is entirely exhausted during those seasons. One possible reason for this discrepancy is the omission of horizontal advection of nutrients in the model. Figure I-4 shows that both nitrate and phosphate divergences for summer and fall have positive values (influx) in the surface layer and negative values (outflux) below the surface. This vertical structure supports surface enrichment and deep depletion of nutrients, which could mitigate the surface phosphate deficiency and the sharper nutricline predicted by the model. However, the magnitude of the nutrient divergence calculated from climatological fields may be too large since our tests showed that they cause excessive accumulation near the

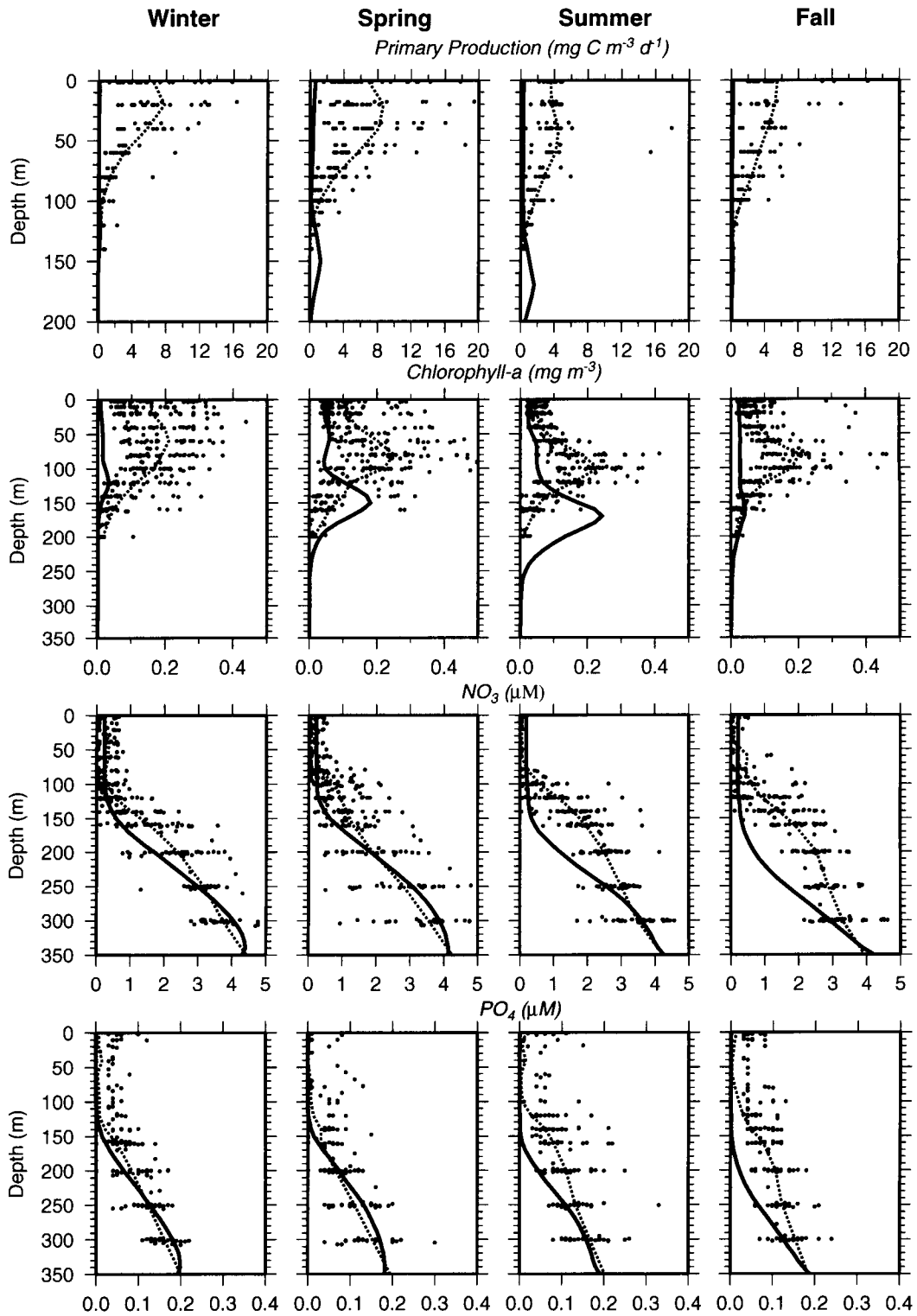


Figure I-6. Seasonal profiles of primary production, chlorophyll, nitrate, and phosphate from run (1). The solid lines are model simulations while the black dots and dashed lines are observations.

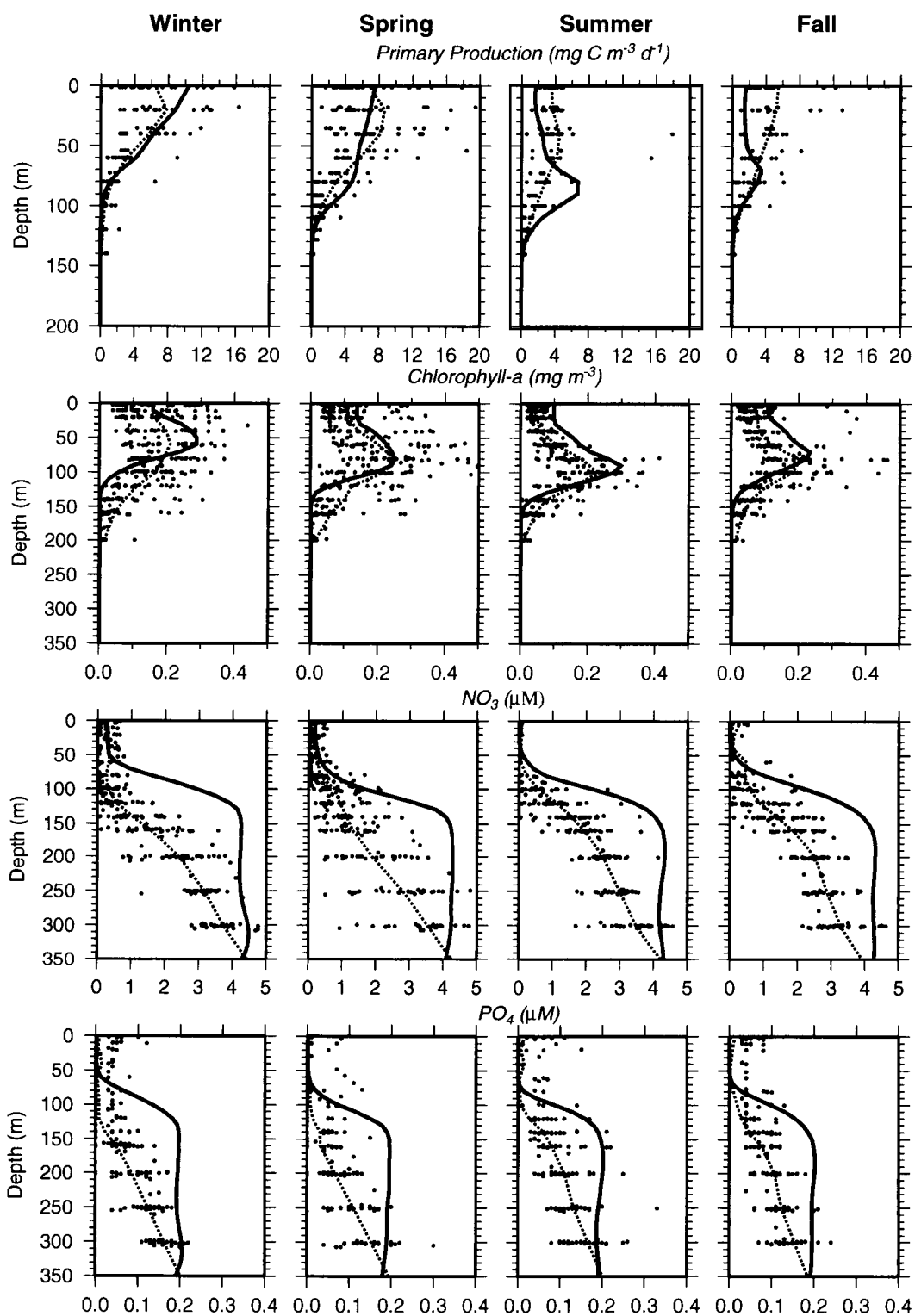


Figure I-7. Seasonal profiles of primary production, chlorophyll, nitrate, and phosphate from run (2). The solid lines are model simulations while the black dots and dashed lines are observations.

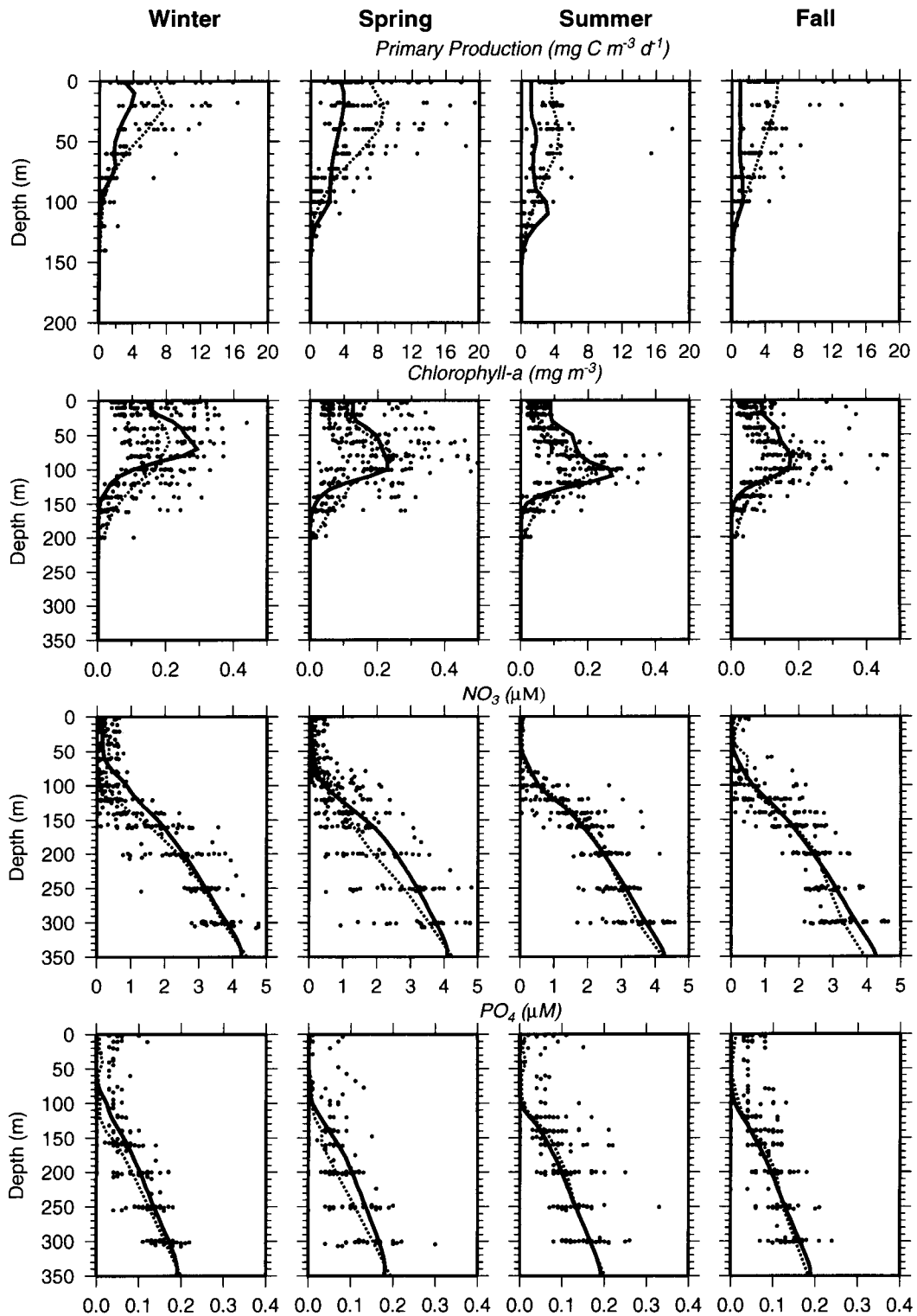


Figure I-8. Seasonal profiles of primary production, chlorophyll, nitrate, and phosphate from run (3). The solid lines are model simulations while the black dots and dashed lines are the observations.

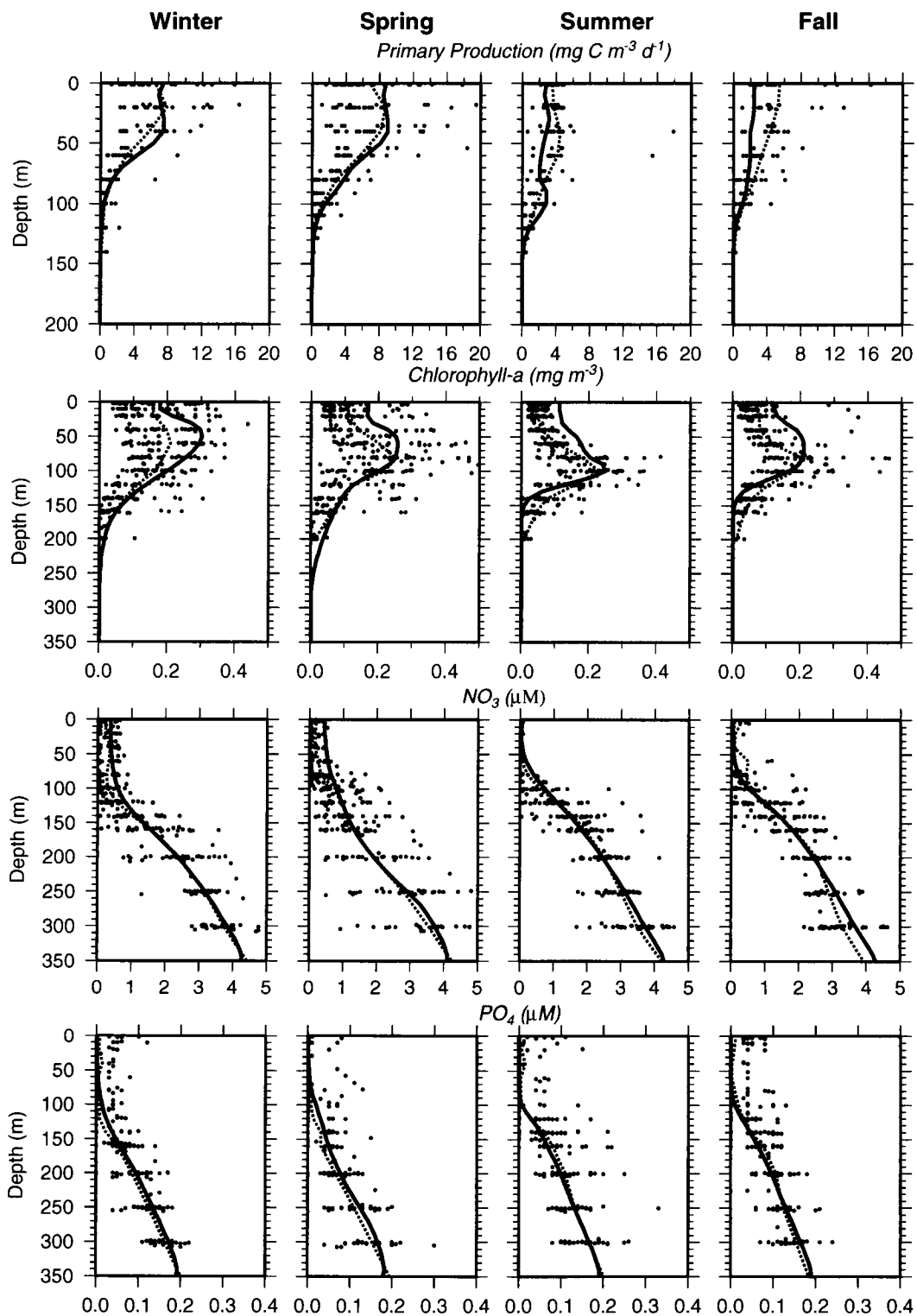


Figure I-9. Seasonal profiles of primary production, chlorophyll, nitrate, and phosphate from run (4). The solid lines are model simulations while the black dots and dashed lines are observations.

surface and too much depletion at depth. In addition, a comparison between runs 1 and 2 shows the importance of the eddy pumping effect on the vertical flux of nutrients. These runs indicate that two extremes in the magnitude of the vertical flux of nutrients are achieved by the use of the two approaches for vertical eddy velocity. The adaptation of the Siegel *et al.* [1999] method for eddy pumping into the model provides reasonable results (although the nutricline is unrealistically sharp), while the use of unconstrained (positive and negative values) eddy vertical velocity does not provide sufficient pumping of nutrients into the euphotic zone. Short of developing an ad hoc vertical velocity approach tuned for the BATS site, the appropriate parameterization of eddy pumping in the model remains an elusive task. However, note that the vertical diffusivity is weakest in summer and fall and, despite the strong subsurface gradients of nitrate and phosphate being too high, the nutrient flux to the surface remains too low. This seems to indicate an inadequate penetration of mixing, demonstrated by the results of run 4, which will be analyzed in the forthcoming discussion.

Figure I-8 shows the profiles from run 3, which includes a relaxation of the nitrate and phosphate concentrations to the climatological profiles below 100m. This relaxation is a proxy to the nutrient horizontal divergence that could not be accurately derived from the climatological data. As shown in Figure I-8, the nutrient profiles simulated in this run are in better agreement with the data. However, the model primary production is low in all seasons. This result leads to the conclusion that mixing in the model is too shallow during winter-spring and therefore limits nutrient supply. The reconfiguration of the eddy diffusivity profile for run 4 was designed to test the hypothesis of shallow mixing. Figure I-9 shows the seasonal profiles obtained from run 4. All model profiles agree well with the data, except for the fall primary production, which is underestimated by the model but not as much as in the two previous runs. Although the reconfiguration of the eddy diffusivity provides the best parameterization for vertical mixing, it violates conservation of TKE in the TCMLM. As shown in equation (6), changing the eddy diffusion profile imparts in a change of buoyancy production (BP), as shown by

$$BP = -\frac{g}{\rho} \overline{w' \rho'} = -\frac{g}{\rho} k_h \frac{\partial \rho}{\partial z} \quad (51)$$

As indicated in equation (51), a change in eddy diffusivity ( $k_h$ ) results in a change of BP and, therefore, a violation of TKE conservation. In view of this, even though the results of run 4 show a significant improvement on the performance of the ecosystem model, and they highlight a deficiency of the TCMLM, the procedure for reconfiguring the eddy diffusivity profile it is not internally consistent. Therefore, run 4 was not used in the final analysis. Instead, the results from run 2 will be used in the forthcoming analyses because no constraints were imposed on the nutrient computation and the eddy diffusivity obtained from the TCMLM is internally consistent.

#### *Nitrate Balance and the Relative Importance of Vertical Mixing and Advection*

The model nitrate balance in the upper 100m for the period of 1992-1997, during which there are available in situ concurrent observations of nutrients, primary production, and



chlorophyll concentration, is summarized in Table I-4. The nitrate balance is calculated for the five different sensitivity runs, based on the model's nitrate conservation equation (equation 25). Values from the literature are tabulated for available parameters. These include results from the eddy-resolving model of *Oschlies* [2002], and the statistical method of *Siegel et al.* [1999] based on altimeter data.

The goal of this analysis is to quantify the relative roles of vertical mixing and vertical advection from mesoscale eddies on the nutrient supply to the euphotic zone. Table I-3b tabulates the nitrate flux for each term of equation 25 (nitrate uptake, ammonium remineralization, nitrogen-fixers (NF) respiration, vertical advection, and vertical mixing) for each of the five runs. The last column shows the ratio of mixing to advection. The NF respiration is relatively negligible. In order of importance, the main supply of nitrate is partitioned among vertical mixing, vertical advection, ammonium remineralization, and NF respiration. The ratio of mixing to advection varies widely from run to run. For the two runs that match the reported estimate of nitrate uptake of  $0.515 \text{ mol N m}^{-2}\text{yr}^{-1}$  [*Siegel et al.*, 1999] for the Sargasso Sea more closely, runs 2 ( $0.592 \text{ mol N m}^{-2}\text{yr}^{-1}$ ) and 4 ( $0.432 \text{ mol N m}^{-2}\text{yr}^{-1}$ ), the mixing to advection ratios are 1.2 and 4.5, respectively. Run 2 was forced with vertical velocity obtained with the upwelling-only mode and no relaxation to climatological nitrate concentration, while run 4 was conducted with relaxation to the climatological nitrate profile below 100m and the use of the ad-hoc eddy diffusivity profile, which provides more robust vertical mixing. The equivalent ratio derived from values of mixing and advection reported by *Siegel et al.* [1999] is 0.9, a value very close to the ratio obtained with run 2. The mixing to advection ratio derived from the eddy-resolving model of *Oschlies* [2002] is 4.4, a value very close to the ratio obtained from run 4 (4.5). However, the model of *Oschlies* [2002], despite its realistic rendition of the mesoscale eddy field, predicts a nitrate uptake ( $0.16 \text{ mol N m}^{-2}\text{yr}^{-1}$ ) for the BATS region that is in the low end of available estimates. *Oschlies* [2002] applied the statistical method of *Siegel et al.* [1999] to his model output at BATS and obtained a value for the vertical advection from mesoscale eddies which is much higher ( $0.180 \text{ mol N m}^{-2}\text{yr}^{-1}$ ) than the value predicted directly from his model ( $0.027 \text{ mol N m}^{-2}\text{yr}^{-1}$ ). These available estimates reveal that there is a large uncertainty in the role of mixing and mesoscale eddies. One of the main reasons for this uncertainty stems from our inability to appropriately parameterize mixing and advection in our models. Despite the good agreement between model and observed SST and MLD, it was not possible to obtain a combination of realistic nutrient profiles and adequate supply of nutrients to the euphotic zone. A key element to resolve this problem is the design of field experiments at the time series sites (i.e., BATS and HOT) that will allow the determination of upper ocean (0-300m) eddy diffusivity profiles. More specifically, the shape of the eddy diffusivity profile within the mixed layer itself, and within the layer separating the base of the mixed layer from the more quiescent ocean below, must be determined to appropriately model vertical mixing. This is especially important for models with high vertical resolution such as the one used in this TM. The uncertainty in determining the shape and magnitude of the vertical velocity profiles derived from satellite altimetry is also a problem. These uncertainties will remain unresolved until new model parameterizations and field experiments can improve the realism of the physical forcing.

### *Biomass, Phytoplankton Nitrogen Production, and Variability of Phytoplankton Growth*

A common result of the sensitivity runs is that for most runs (except for run 1) the predicted biomass concentration matched the observations despite very low predicted primary production in 3 out of the five runs. To further investigate this apparent inconsistency, an analysis of the upper-100m phytoplankton nitrogen flux (1992-1997 mean) was conducted based on the balance of the source and sink terms in equation 20. The results are shown in Table I-5. The phytoplankton nitrogen production is balanced, in order of importance, by zooplankton grazing, phytoplankton respiration and mortality, and physical transport by vertical advection and mixing. The physical transport is relatively small in all runs. The biomass and primary production are tabulated for all runs. The derived phytoplankton nitrogen production and phytoplankton biomass, are also shown in Table I-5 (see footnotes in Table I-5 for explanation on how phytoplankton nitrogen production and biomass were derived).

The main result from this analysis is that there is a large variability of phytoplankton nitrogen production and grazing while the mortality, respiration, and biomass do not significantly change relative to growth and grazing. This indicates that the model biomass is under strong grazing control. This result is consistent with the behavior of the grazing, mortality, and respiration terms in equation 20. The zooplankton grazing term (equation 35) is proportional to the square of the biomass, while respiration and mortality (equation 20) are a linear function of the biomass. Therefore, it is possible to have low growth and reasonable values of biomass in the model, such that the model results must be evaluated for both biomass and primary production to accomplish a stringent validation test. For instance, run 2 is the only run that provides a combined reasonable match of new production ( $0.59 \text{ mol N m}^{-2} \text{ yr}^{-1}$ ), total phytoplankton nitrogen production ( $1.84 \text{ mol N m}^{-2} \text{ yr}^{-1}$ ), and biomass ( $14.8 \text{ mol N m}^{-2}$ ) with the available observed values. The corresponding observed values for the BATS region are  $0.52 \text{ mol N m}^{-2} \text{ yr}^{-1}$ ,  $1.87 \text{ mol N m}^{-2} \text{ yr}^{-1}$ , and  $13.6 \text{ mol N m}^{-2}$ , respectively.

An additional test was conducted to verify that the model formulations for the sources and sinks of phytoplankton nitrogen are appropriate for the BATS region. This was achieved by calculating the ratio of the standard deviation of the surface phytoplankton growth ( $\mu$ , in  $\text{d}^{-1}$ ) to the standard deviation of surface chl-a concentration ( $\text{mg m}^{-3}$ ) for the model and observations. The standard deviations of both model and observations are based on the period 1992-1997. We calculate the phytoplankton growth from observed primary production (PP) and chl-a concentration at BATS using the formula  $\mu(\text{d}^{-1}) = (\text{PP chl:N}) / (12 \text{ C:N chl-a})$ . The fixed C:N ratio (6.625) and the surface chl:N ratio (0.8) are the same values used in the model. The constant 12 is the molecular weight of carbon. The ratio of surface growth to surface chl-a standard deviations using values from run 2, which provided the best combined match of new production, phytoplankton nitrogen production, and biomass with the equivalent parameters derived from the BATS data, is  $4.1 \text{ d}^{-1} (\text{mg chl-a m}^{-3})^{-1}$ . The equivalent ratio derived from the

BATS data is  $4.5 \text{ d}^{-1} (\text{mg chl-a m}^{-3})^{-1}$ , which is 9.8% higher than for run 2. The similarity between model and data ratios shows that the balance between phytoplankton growth and biomass is accurately represented by the model dynamics.

**Table I-4.** Model nitrate balance in the upper 100m (1992-1997) from five different runs. Runs 1,2,3, and 5 use  $k_r$  from the TCMLM. Run 4 uses  $k_r$  from the ad-hoc approach described in the text. Runs 1 and 5 are forced with unconstrained vertical velocity (upwelling/downwelling mode), while all the other runs are forced with upwelling-only mode (Siegel *et al.*, 1999). Relaxation to nitrate and phosphate climatology below 100m was imposed only for runs 3,4, and 5. All units are in  $\text{mol N m}^{-2} \text{ yr}^{-1}$ . Values from the literature are tabulated for available parameters.

Source	NO <sub>3</sub> Uptake	NH <sub>4</sub> Rem.	NF Respiration	Vertical Advection	Vertical Mixing	Mixing Advection
Run 1	-0.057	0.020	0.00040	0.006	0.031	5.2
Run 2	-0.592	0.029	0.00006	0.251	0.312	1.2
Run 3	-0.224	0.026	0.00003	0.080	0.118	1.5
Run 4	-0.432	0.030	0.00005	0.073	0.329	4.5
Run 5	-0.171	0.020	0.00003	0.053	0.098	1.8
<i>Oschlies</i> , 2002	-0.16*			0.027	0.120	4.4
<i>Oschlies</i> , 2002				0.180***		
<i>Siegel et al.</i> , 1999	-0.515**			0.240	0.215	0.9

\* Balance of  $0.013 \text{ mol N m}^{-2} \text{ yr}^{-1}$  due to other processes not reported in paper.

\*\* Includes Ekman horizontal flux and atmospheric deposition ( $0.06 \text{ mol N m}^{-2} \text{ yr}^{-1}$ ).

\*\*\* Application of statistical method of Siegel *et al.* [1999] to 3D model output by *Oschlies* [2002].

**Table I-5.** Model phytoplankton nitrogen balance in the upper 100m (1992-1997) resulting from the five different runs described in the text and in the caption for Table I-4. The integrated (0-100m) biomass is also tabulated for each run. The last column shows the corresponding observed phytoplankton nitrogen production at BATS, and phytoplankton biomass derived from the observed chlorophyll concentration. The model phytoplankton balance does not include nitrogen-fixing phytoplankton (equation 20). All units are in  $\text{mol N m}^{-2} \text{ yr}^{-1}$ , except for the integrated biomass, which is in  $\text{mol N m}^{-2}$ .

	Run 1	Run 2	Run 3	Run 4	Run 5	Data
Phyto N Prod	0.855	1.844	0.873	1.381	0.736	1.874*
Grazing	-0.551	-1.192	-0.331	-0.659	-0.250	
Respiration	-0.146	-0.271	-0.246	-0.274	-0.224	
Mortality	-0.146	-0.271	-0.246	-0.274	-0.224	
Advection	-0.003	-0.006	-0.005	-0.006	-0.005	
Mixing	-0.028	-0.100	-0.046	-0.165	-0.038	
Biomass	8.0	14.8	13.5	15.0	12.3	13.6**

\* Phytoplankton nitrogen production is calculated from observed primary production (PP in  $\text{mg C m}^{-3} \text{ d}^{-1}$ ):

Phyto N Prod =  $\frac{0.365}{12 \text{ C:N}} \int_{-100}^0 \text{PP } dz$ , where C:N = 6.625 is the Redfield ratio and 12 is the molecular weight of carbon. The coefficient 0.365 converts  $\text{mmol N m}^{-2} \text{ d}^{-1}$  to  $\text{mol N m}^{-2} \text{ yr}^{-1}$ .

\*\* Biomass is calculated from observed chl-*a* ( $\text{mg m}^{-3}$ ) and chl:N ratio ( $\text{mg chl-}a/\text{mmol N}$ ) from model (Run 2):

$$P = \int_{-100}^0 \frac{\text{chl-}a}{\text{chl:N}} dz$$

### *Model Validation and Comparison with Previous Model*

With a few exceptions, the model results (run 2) match the observations very well. Figure I-10 shows a comparison between the predicted (solid line) seasonal profiles of temperature and salinity with corresponding observed values (black dots). The seasonal thermocline, the surface temperature, and surface salinity, are accurately represented by the model. Seasonal profiles of the predicted biogeochemical parameters are shown in Figures I-7 and I-11. The overall agreement with the data is good with the exception of the summer-fall primary production, which is underestimated by the model, and, as explained in the previous section, a much sharper nutricline when compared to the observed nitrate and phosphate profiles. The seasonal profiles of  $\text{TCO}_2$ ,  $\text{O}_2$ , DON and DOC compare well with observations, except for the winter DON, which is underestimated by the model.

Time series of model (red lines) and observed (green lines for in situ data and blue lines for satellite data) chlorophyll concentration and primary production are shown in Figure I-12. The model series is daily, while the in situ data were obtained on a nearly monthly basis. The satellite data are from monthly composites. The timing of the spring bloom is well represented by the model. Again, it is quiet clear that the model under-predicts the summer-fall primary production. The predicted chlorophyll concentration tracks the observed values well, except for the 1995 spring transition where the fluorometric chlorophyll measurements have a few high values (as high as nearly  $0.7\text{mg m}^{-3}$ ). The satellite-derived (OCTS and SeaWiFS) chlorophyll concentrations are from monthly composites and therefore are much smoother but still in good agreement with the in situ data. Note that the OCTS and model records in early 1997 show anomalous high values compared to in situ data. Otherwise, monthly mean satellite values during peaks are low.

Figure I-13 shows time series of model (solid) and predicted (dashed) SST and surface  $\text{TCO}_2$ , calculated alkalinity (regressed on salinity), and predicted  $\Delta\text{pCO}_2$  and sea-air  $\text{CO}_2$  flux. The surface alkalinity concentrations calculated from the model salinity (solid) and from the observed salinity (dashed) are very close because the model surface salinity is strongly relaxed to observed values. The model (solid) and observed (dashed)  $\text{TCO}_2$  trends are very similar ( $1.3$  and  $1.2\ \mu\text{mol kg}^{-1}\ \text{yr}^{-1}$ , respectively). The predicted seasonal and interannual variability in  $\text{TCO}_2$  concentration compares well with the observed values, except when the predicted SST differs from observations. This is evident during the 1995, 1996, and 1997 winters, during which the predicted SST is warmer than observations. Also, notice that the model  $\text{TCO}_2$  is biased low when compared to the data ( $-3\ \mu\text{mol kg}^{-1}$ ). This bias is a result of a corresponding bias in the model SST ( $+0.48^\circ\text{C}$ ), probably due to a bias in the total surface heat flux. The time series of predicted sea-air  $\text{CO}_2$  flux shows larger ingassing during winter than outgassing during summer, despite a nearly symmetric summer-winter  $\Delta\text{pCO}_2$ . This can be explained by the larger wind speeds attained during winter months when the sea-air  $\Delta\text{pCO}_2$  reaches its maximum negative value and the sea-air flux reaches its peak ingassing.

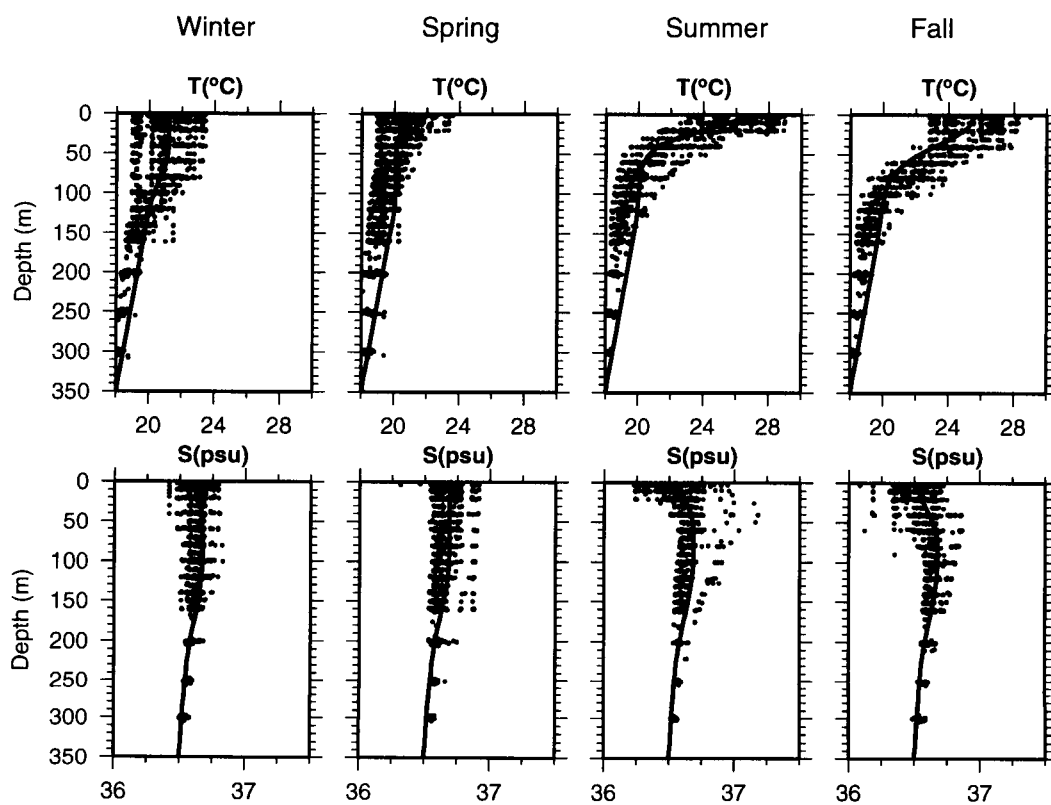


Figure I-10. Seasonal profiles of model (solid lines) and observed (black dots) temperature and salinity.

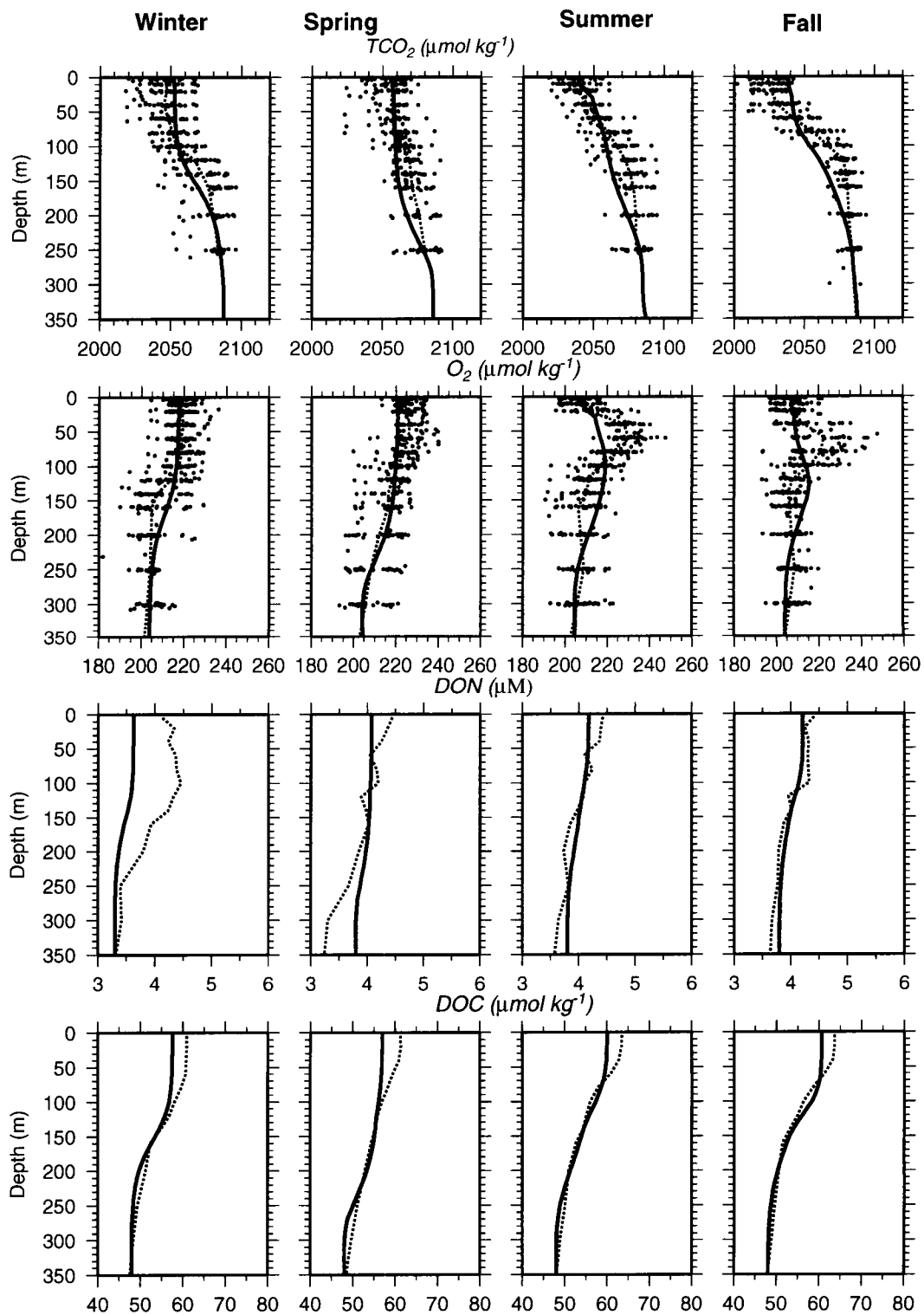


Figure I-11. Seasonal profiles of  $\text{TCO}_2$ ,  $\text{O}_2$ , DON, and DOC. The solid lines are model profiles (run 2), while the black dots and dashed lines are observed profiles.

Blue=SeaWiFS and OCTS Chlorophyll at BATS Site  
 Green with Black Crosses=Observed at BATS (32.25°N, 65.75°W)  
 Red=Model

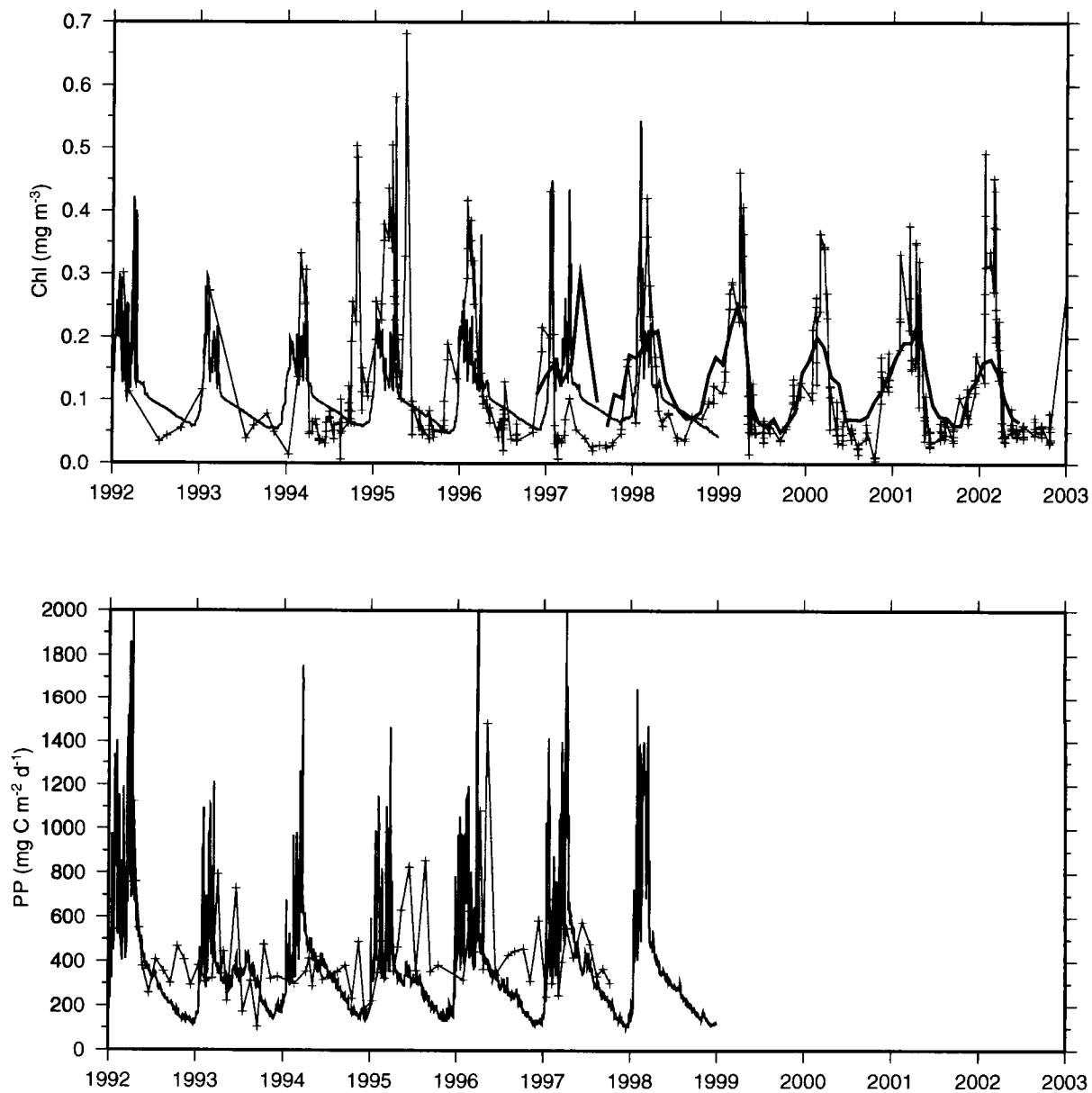


Figure I-12. Time series of OCTS and SeaWiFS (blue), observed (green), and model surface chlorophyll at the BATS site.

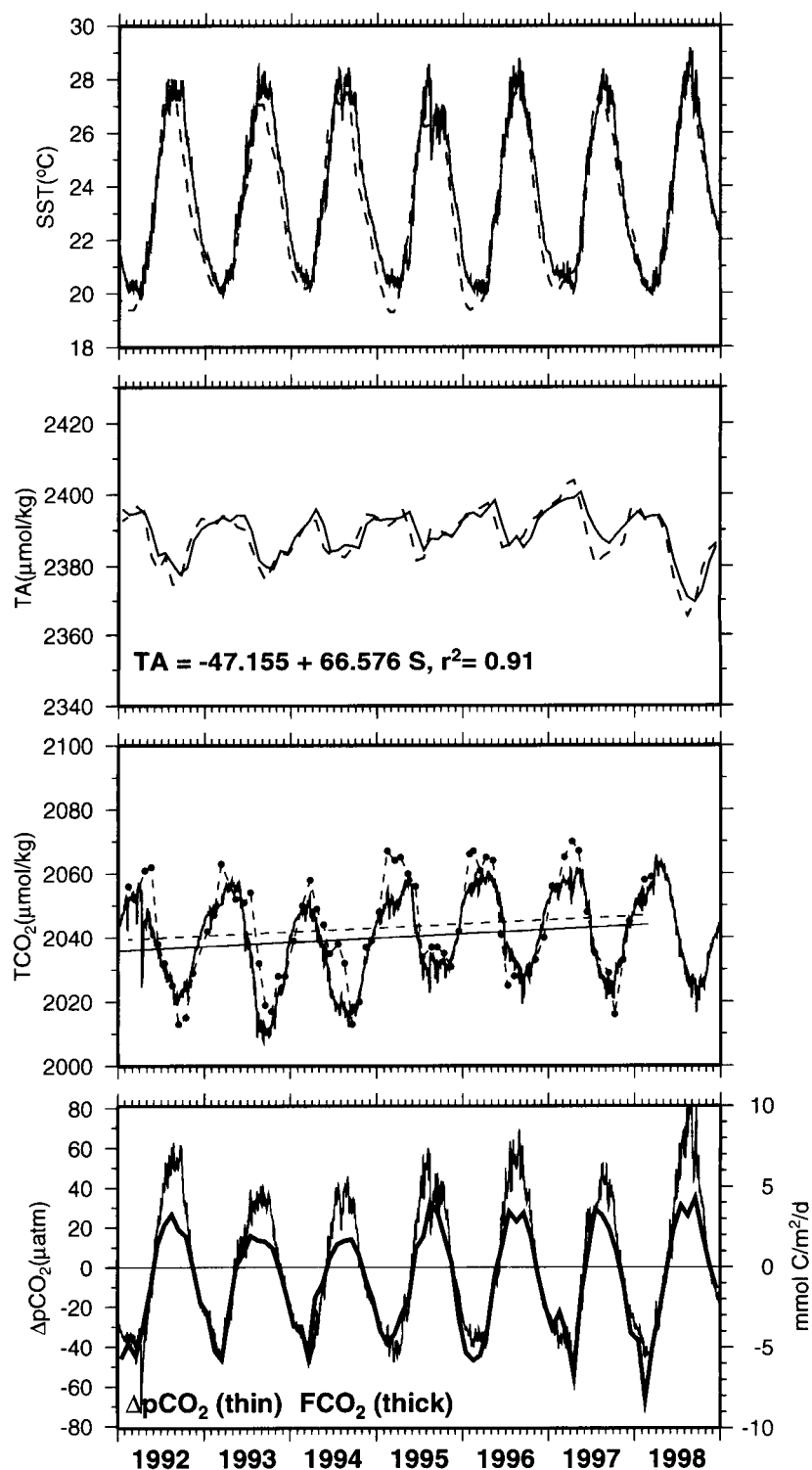


Figure I-13. Time series of SST, alkalinity (TA), TCO<sub>2</sub>, ΔpCO<sub>2</sub>, and sea-air CO<sub>2</sub> flux (FCO<sub>2</sub>). The model time series are shown as solid lines whereas the observed time series are shown as dashed lines. The TA dashed line represents a regression to salinity, not the observed values which are not available.



Figure I-14 shows the predicted (solid line) and measured (black dots)  $\Delta p\text{CO}_2$  for years 1994 and 1995. Predictions from both the previous (bottom) and current (top) models are shown. Some degree of improvement seems to be achieved with the current model, especially during 1995. Table I-6 summarizes seasonal and climatological comparisons between predicted and observed biogeochemical parameters. Predicted values are tabulated for the previous and current models. The values labeled with asterisks denote improved matches between observations and the current model predictions. The improvements vary with parameter and season. There were improvements in the model simulation of chlorophyll, PAR, nitrate, DOC, primary production, and oxygen, but most importantly, the current model achieved good agreement with the data with much more realistic background eddy diffusivity. The current model used a constant value of  $5 \times 10^{-5} \text{ m}^2 \text{ s}^{-1}$ , while the previous version used variable background eddy diffusivity ranging from  $5 \times 10^{-5} \text{ m}^2 \text{ s}^{-1}$  to  $58 \times 10^{-5} \text{ m}^2 \text{ s}^{-1}$ .

**Table I-6.** Summary of seasonal and climatological (1992-1998) comparisons between predicted and observed biogeochemical parameters. The second line for each parameter tabulates the results from the new model. The asterisks highlight values from the new model for which noticeable improvement was achieved.

	Winter		Spring		Summer		Fall		Year	
	Model	Data	Model	Data	Model	Data	Model	Data	Model	Data
PAR	46.0	49.3	83.5	89.8	96.3	99.2	61.5	68.9	71.8	76.8
	46.4		86.5*		99.8*		63.1		74.0*	
Chl- <i>a</i>	0.14	0.16	0.14	0.11	0.11	0.04	0.12	0.07	0.13	0.10
	0.16*		0.14		0.11		0.12		0.13	
NO <sub>3</sub>	0.43	0.26	0.64	0.16	0.16	0.06	0.09	0.16	0.33	0.16
	0.51		0.33*		0.06*		0.15*		0.26*	
PO <sub>4</sub>	0.012	0.009	0.017	0.003	0.002	0.010	0.003	0.008	0.009	0.008
	0.002		0.002*		0.000		0.000		0.001	
PP	456	432	657	593	440	382	375	387	482	449
	550		617*		411*		218		449*	
DON	4.5	4.4	4.4	4.4	4.5	4.4	4.5	4.3	4.5	4.4
	3.7		4.2		4.2		4.3*		4.1	
DOC	61.5	60.9	60.6	61.1	61.8	63.3	62.2	63.5	61.5	62.2
	58.0		57.2		60.0		61.5		59.2	
TCO <sub>2</sub>	2049	2046	2058	2055	2037	2036	2030	2024	2044	2040
	2053		2056*		2038		2039		2047	
O <sub>2</sub>	223	218	224	224	207	206	208	207	216	214
	220*		224		208		207*		215*	

Nitrate, Phosphate, DON, DOP ( $\text{mmol m}^{-3}$ ), and DOC ( $\mu\text{mol kg}^{-1}$ ) were averaged from the surface to 50m. The Chl-*a* ( $\text{mg m}^{-3}$ ), TCO<sub>2</sub> ( $\mu\text{mol kg}^{-1}$ ), O<sub>2</sub> ( $\mu\text{mol kg}^{-1}$ ) concentrations are surface values. The observed surface irradiance (PAR, in  $\text{W m}^{-2}$ ) is obtained from 1992-1997 averages. The primary production (PP in  $\text{mg C m}^{-2} \text{ d}^{-1}$ ) is integrated from surface to 150m for the period of 1992-1997.

### Carbon Budget

Figure I-15 shows the mean carbon balance for the BATS region based on the 7-year (1992-1998) model simulation. The two boxes in Figure I-15 represent the dissolved inorganic carbon (DIC) in surface water (solubility pump), and the biological pump, which takes up CO<sub>2</sub> from the DIC pool via photosynthesis and exports POC and DOC as

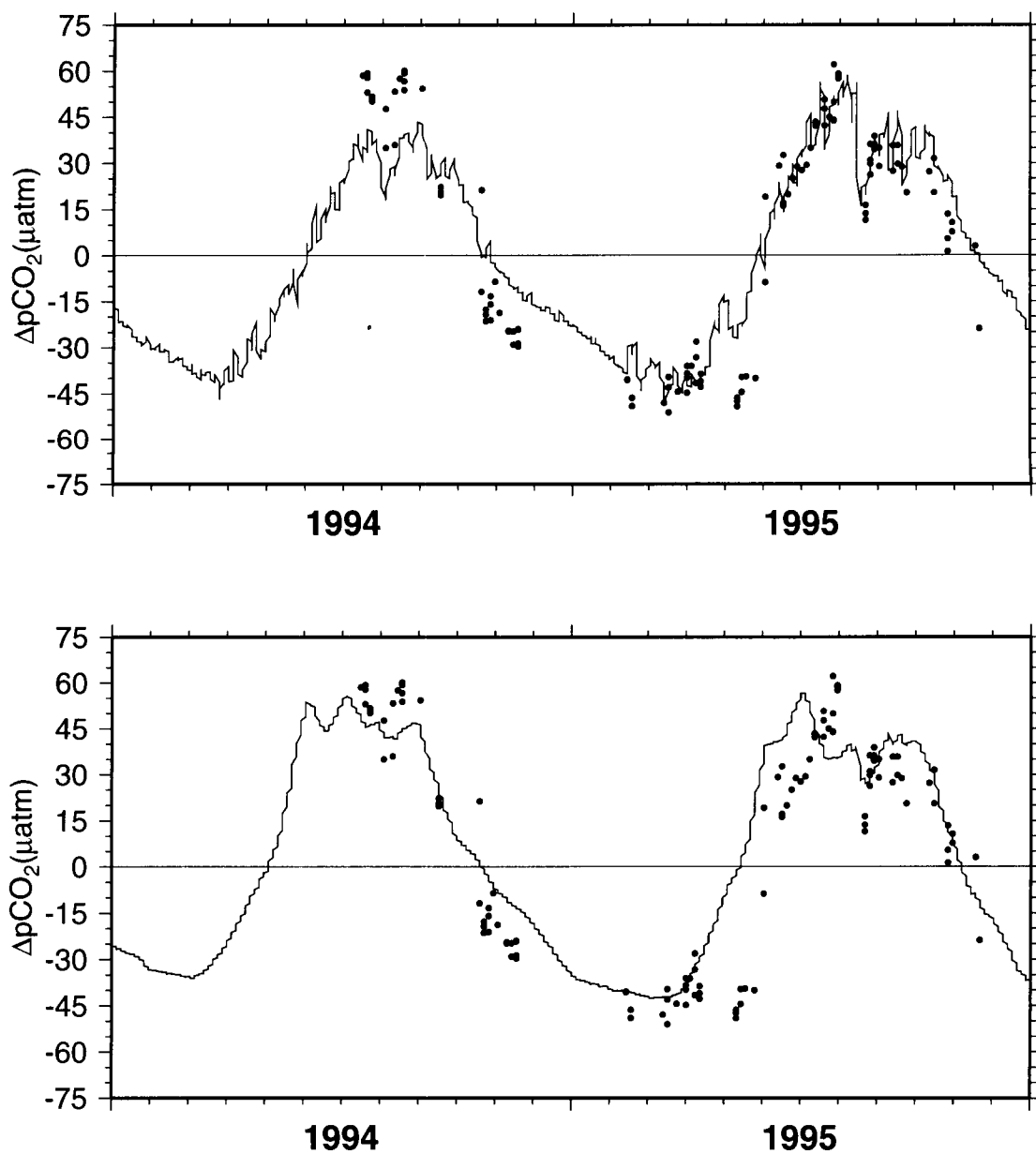


Figure I-14. Time series of model (solid lines) and observed (black dots)  $\Delta p\text{CO}_2$ . The top tier show the series from the current model, whereas the bottom tier show the series from the previous model.

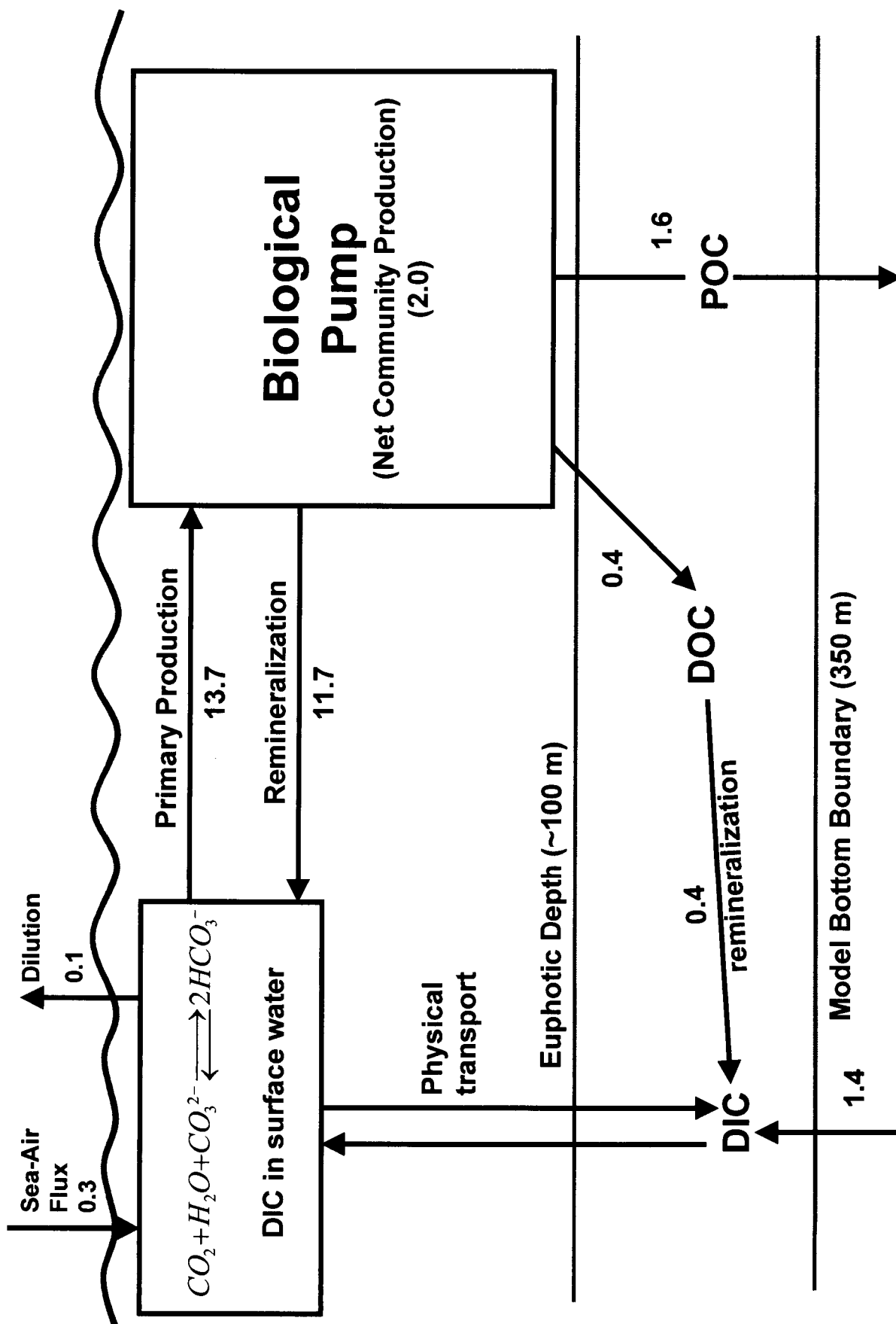


Figure I-15: Averaged (1992-1998) carbon balance for the BATS study area. Fluxes are in  $\text{mol C m}^{-2} \text{ yr}^{-1}$ . The dilution term is effectively a result of freshwater flux (precipitation minus evaporation).

byproducts. The DOC is remineralized into DIC at a rate of  $0.4 \text{ mol C m}^{-2} \text{ yr}^{-1}$ . The biological DIC consumption, i.e., the net community production ( $2.0 \text{ mol C m}^{-2} \text{ yr}^{-1}$ ), is balanced by the air-sea  $\text{CO}_2$  flux ( $0.3 \text{ mol C m}^{-2} \text{ yr}^{-1}$ ), DIC dilution ( $-0.1 \text{ mol C m}^{-2} \text{ yr}^{-1}$ ), remineralization of DOC ( $0.4 \text{ mol C m}^{-2} \text{ yr}^{-1}$ ), and the DIC flux ( $1.4 \text{ mol C m}^{-2} \text{ yr}^{-1}$ ) at the bottom boundary (350 m). In terms of overall carbon balance, the sedimentation rate (POC export),  $1.6 \text{ mol C m}^{-2} \text{ yr}^{-1}$ , is balanced by the air-sea  $\text{CO}_2$  flux and the DIC physical transport through the bottom boundary.

### *Conclusions*

The use of the TCMLM contributed to some improvements in the model simulation of chlorophyll, PAR, nitrate, phosphate, and oxygen, but most importantly, the current model achieved good agreement with the data with much more realistic background eddy diffusivity. However, sensitivity tests showed that the TCMLM does not provide adequate vertical mixing (convective mixing is  $\sim 50\text{m}$  shallower than indicated by the data) in winter-spring. In addition, off-line calculations of horizontal divergence of nutrients, heat, salt, and dissolved inorganic carbon, using seasonal climatologies, revealed that the BATS site lies in a region where horizontal transport of physical and biogeochemical properties by the ambient flow is an important process that cannot be neglected in studies of nutrient, biomass, and carbon balances. Also, mesoscale eddies play an important role in the vertical transport of nutrients (eddy pumping) to the euphotic zone, as shown by several previous studies in the region [McGillicuddy *et al.*, 1999; McGillicuddy *et al.*, 1998b; Siegel *et al.*, 1999]. The role of these eddies on the horizontal transport of nutrients, and other biogeochemical properties, remains unquantified. Therefore, future studies in the BATS region will require comprehensive three-dimensional field studies, combined with three-dimensional eddy resolving numerical experiments, to adequately quantify the impact of the local and remote forcing on ecosystem dynamics and carbon cycling.

## Chapter II

### Sensitivity of Global Sea-Air CO<sub>2</sub> Flux to Gas Transfer Algorithms, Climatological Wind Speeds, Sea Surface Temperature, and Salinity

#### II.1. Background

The global sea-air flux of CO<sub>2</sub> is strongly dependent on the sea-air  $p\text{CO}_2$  difference ( $\Delta p\text{CO}_2$ ) and the gas exchange coefficient. These two components of the air-sea flux have similar ranges of variability in the ocean and, therefore, are equally important in determining the accuracy of the estimated flux. The gas exchange coefficient is primarily a function of the wind speed [Liss and Merlivat, 1986; Tans *et al.*, 1990; Wanninkhof, 1992], but the ocean  $p\text{CO}_2$  is highly dependent on temperature and salinity. The ocean  $p\text{CO}_2$  is a function of the total carbon dioxide (TCO<sub>2</sub>) concentration, the total alkalinity (TA), and dissociation constants for the chemical components of the CO<sub>2</sub> system. [Dickson and Millero, 1987; Signorini and McClain, 2002; Signorini *et al.*, 2001a; Signorini *et al.*, 2001b]. The dissociation constants are functions of temperature and salinity [Dickson and Millero, 1987]. The distribution of surface alkalinity in the open ocean is mainly controlled by the factors that govern salinity [Millero *et al.*, 1998]. Therefore, accurate measurements of seasonal and interannual changes of surface salinity and temperature of the world's oceans are central to studies of global carbon flux. The biological uptake of CO<sub>2</sub> is also an important component of the carbon cycle in the oceans. However, in this study we do not explicitly address the effect of biological uptake of CO<sub>2</sub>. It is assumed that the biological effect is implicitly included in the climatological TCO<sub>2</sub> seasonal fields used here.

#### II.2. Methodology and Data Sources

This study is a revision of the approach used by Signorini and McClain [2002]. There were two major changes from the previous study. The Wanninkhof [1992] gas transfer algorithm now uses the 0.39 coefficient for climatological winds instead of the 0.31 coefficient for short winds. Now the Wanninkhof [1992] and Tans *et al.* [1990] algorithms yield very similar results. Also, the DIC values are no longer kept constant when changes of SST and SSS are made. The algorithm of Lee *et al.* [2000] is used for calculating changes in DIC due to variations in SST and SSS. This modification on the computational strategy resulted in more internally consistent analyses.

We used an ocean  $p\text{CO}_2$  model [Signorini *et al.*, 2001a; Signorini *et al.*, 2001b], combined with algorithms for TA, TCO<sub>2</sub>, and gas transfer, to estimate the seasonal sea-air CO<sub>2</sub> flux for the global oceans. The required input data for the ocean  $p\text{CO}_2$  model are SST, SSS, TA, and TCO<sub>2</sub>. The normalized seasonal alkalinity (NTA) was obtained from the algorithm of Millero *et al.* [1998], which is a quadratic function of SST. The salinity effect on alkalinity is incorporated via dilution ( $\text{TA} = \text{SSS} \times \text{NTA} / 35$ ). The regression coefficients and reference temperature vary according to specific ocean basins and regional domains [Millero *et al.*, 1998]. The seasonal SST and SSS global fields are from

the World Atlas 1998 [Conkright *et al.*, 1998]. For the purposes of this analysis the TA estimates are assumed to be error-free.

Existing TCO<sub>2</sub> algorithms are still not accurate enough to retrieve required *p*CO<sub>2</sub> values within reasonable limits. Over the global oceans, Δ*p*CO<sub>2</sub> vary from -100 μatm to +100 μatm, (Figure II-1) but its global mean is always between 0 and -6 μatm. An error of 1 μmol/kg in TCO<sub>2</sub> translates into an error of ~1.5 μatm on *p*CO<sub>2</sub>. Lee *et al.* [2000] compared TCO<sub>2</sub> fields obtained with their SST and SSS algorithm to the TCO<sub>2</sub> fields obtained from the combination of Takahashi *et al.* (1997) *p*CO<sub>2</sub> data and TA fields. The differences are very large (±40 μmol/kg). For this reason we computed the TCO<sub>2</sub> seasonal fields from available ocean *p*CO<sub>2</sub> data [Takahashi *et al.*, 1997], seasonal TA fields derived from the Millero *et al.* [1998] algorithm, and SST and SSS from World Atlas 1998 [Conkright *et al.*, 1998] climatology. Therefore, the TCO<sub>2</sub> seasonal fields calculated this way, combined with the TA, SST, and SSS seasonal fields, reproduce the seasonal *p*CO<sub>2</sub> data from Takahashi *et al.* [1997] exactly. The combination of these input data sets was used to perform the sensitivity analysis in this study. The TCO<sub>2</sub> sensitivity to SST and SSS is obtained using the Lee *et al.* [2000] algorithm.

The flux of CO<sub>2</sub> between the atmosphere and ocean is commonly estimated using a bulk formula that relates the flux to the air-sea concentration difference via a gas transfer velocity [Wanninkhof, 1992]:

$$F_{\text{CO}_2} = ks\Delta p\text{CO}_2 \quad (52)$$

where the solubility of CO<sub>2</sub> in seawater (*s*) is included because the difference (Δ*p*CO<sub>2</sub>) is expressed in terms of partial pressures.

Air-sea gas transfer is typically parameterized in terms of a transfer velocity and the gas concentration difference across the air-sea interface. Transfer velocities (*k*<sub>660</sub>) are commonly normalized to a nominal Schmidt number, *Sc*=660, through the following relationship which accounts for differences in gas diffusivity

$$k_{660} = k \left( \frac{660}{Sc} \right)^{-1/2} \quad (53)$$

Figure II-2 shows the normalized transfer velocity (cm hr<sup>-1</sup>) as a function of wind speed (m s<sup>-1</sup>) for six different gas transfer algorithms [Liss and Merlivat, 1986; McGillis *et al.*, 2001; Nightingale *et al.*, 2000; Wanninkhof, 1992; Wanninkhof and McGillis, 1999]. The algorithm of Tans *et al.* [1990], used in this study, is not represented in Figure II-2 because it is not explicitly expressed as a function of transfer velocity; it is expressed as a constant times the wind speed. These six algorithms have quite different behaviors, especially above wind speeds of 8 m s<sup>-1</sup> where they diverge significantly. An in situ evaluation of air-sea gas exchange parameterizations, using conservative and volatile tracers in the southern North Sea, is provided by Nightingale *et al.* [2000]. They concluded that the optimal gas exchange relationship (see Figure II-2) shows a

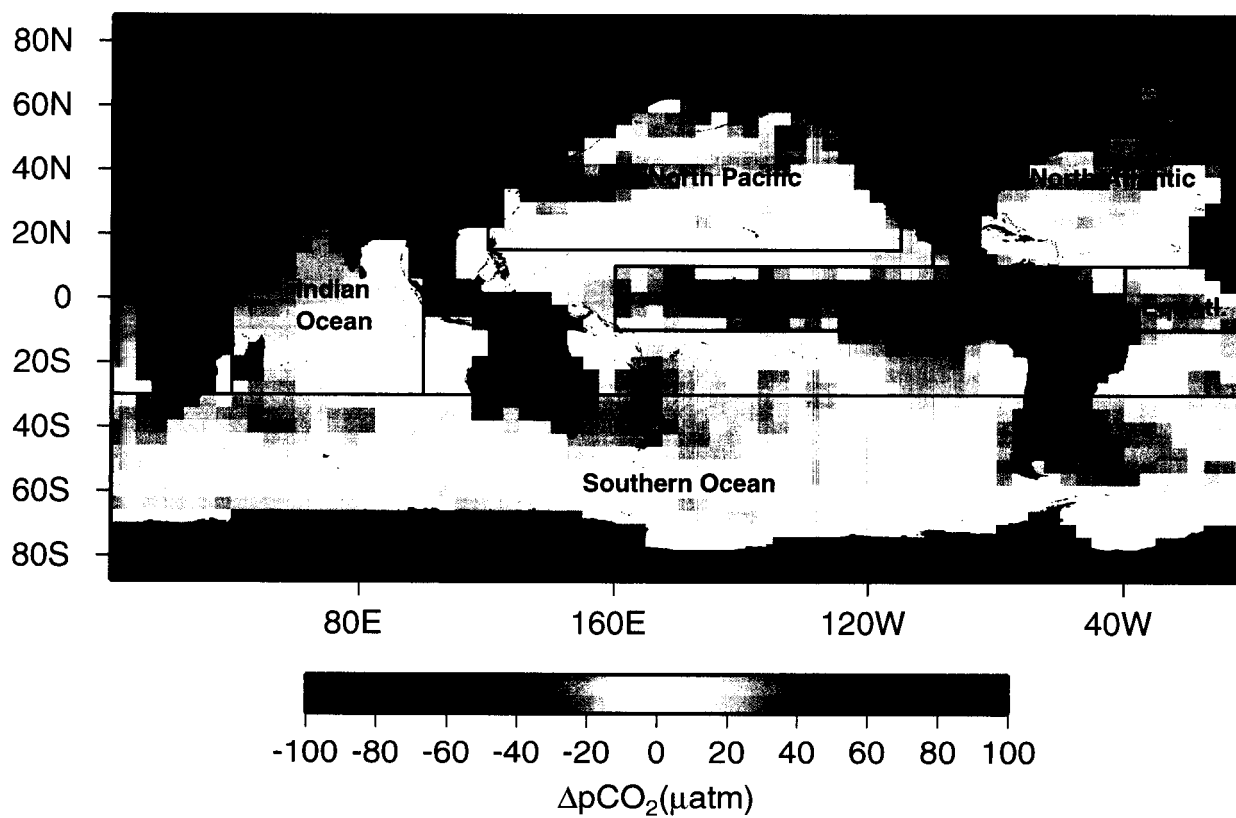


Figure II-1. Global map of annual sea-air  $\Delta p\text{CO}_2$  from *Takahashi et al.* (1997) showing the six sub-regions chosen for analysis.

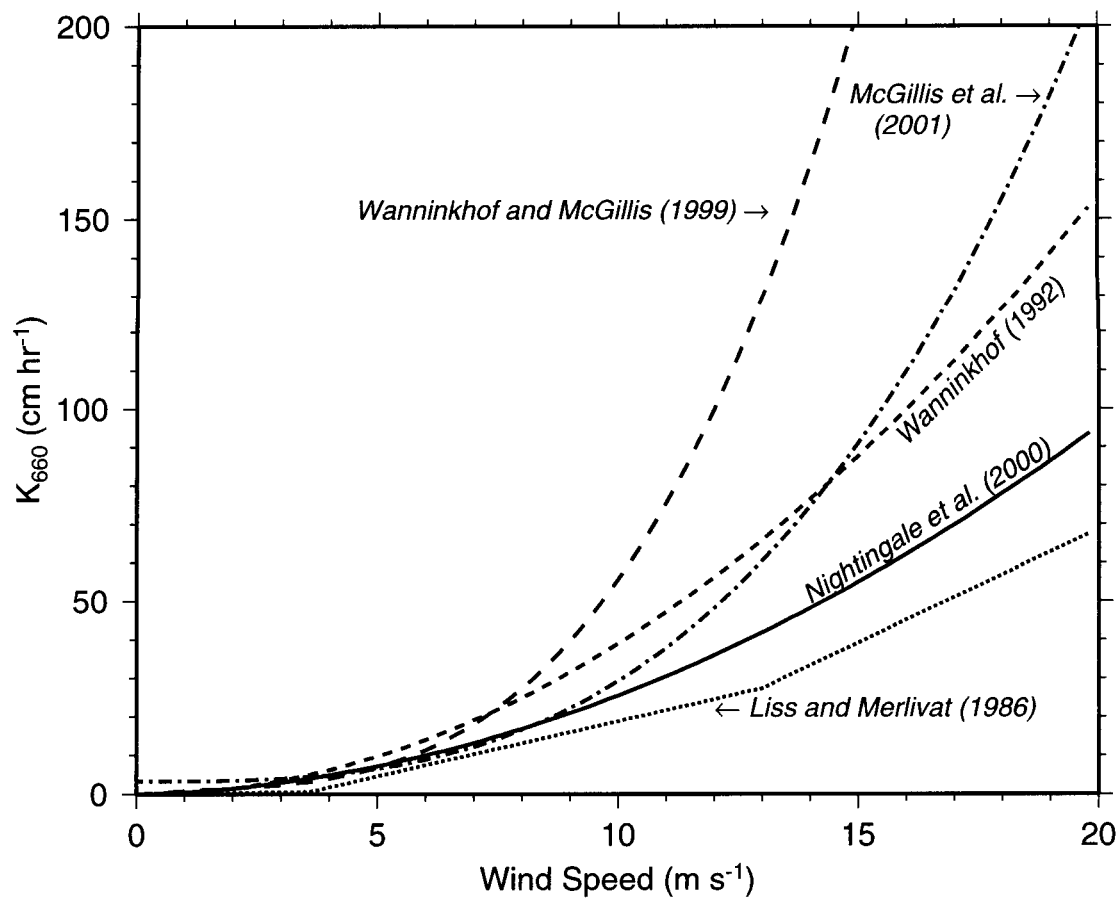


Figure II-2. Gas transfer coefficient as a function of wind speed derived with five different algorithms.



dependence on wind speed intermediate between those of *Liss and Merlivat* [1986] and *Wanninkhof* [1992]. The *Wanninkhof* [1992] algorithm is in agreement with the global mean transfer velocity determined from the oceanic uptake of bomb-derived radiocarbon ( $^{14}\text{C}$ ) [*Broecker et al.*, 1985]. Similarly, *Tans et al.* [1990] adjusted the radon-derived parameterization of [*Smethie et al.*, 1985] to fit through the  $^{14}\text{C}$  value. The *Wanninkhof* [1992] algorithm is also in agreement with the gas exchange study of *Keeling et al.* [1998], which is based on seasonal variations in the atmospheric oxygen/nitrogen ratio. The gas exchange study of *Gabric et al.* [1995], based on mass budgeting of dimethylsulfide, favors the *Liss and Merlivat* [1986] algorithm. More recently, *McGillis et al.* [2001] conducted direct co-variance air-sea  $\text{CO}_2$  flux measurements in the North Atlantic within a significant  $\text{CO}_2$  sink. These direct estimates are also in agreement with the traditional geochemical isotope constraints. However, *McGillis et al.* [2001] show that measurements for winds in excess of  $11 \text{ m s}^{-1}$  indicate a general enhancement of gas transfer velocity over previous indirect measurements. They believe that this enhancement can be explained by the fact that indirect methods cannot discriminate surface process variability such as atmospheric stability, upper-ocean mixing, wave age, wave breaking, or surface films.

The air-sea  $\text{CO}_2$  flux ( $\text{FCO}_2$ ) is calculated in this study using the following four gas transfer algorithms: (I) *Liss and Merlivat* [1986], *Wanninkhof* [1992], *Tans et al.* [1990], and *Wanninkhof and McGillis* [1999]. These four algorithms were chosen because their behaviors span a wide range of gas transfer velocity values and therefore are suitable for the wind speed sensitivity analysis. The seasonal global distribution of atmospheric  $p\text{CO}_2$  for 1990 was obtained from concurrently available data [*Conway and Tans*, 1996] at three sampling sites, Cold Bay ( $55^\circ\text{N}$ ), Mauna Loa ( $19.5^\circ\text{N}$ ), and the South Pole ( $90^\circ\text{S}$ ). The year 1990 was chosen because it is the reference year used by *Takahashi et al.* [1997] to correct the  $p\text{CO}_2$  observations used in their global carbon flux estimates. Therefore, our carbon flux estimates are also for 1990. A latitude-dependent global seasonal distribution of atmospheric  $p\text{CO}_2$  at one-degree resolution was constructed by fitting a spline to the three concurrently available records from the three chosen sites.

Each of the four algorithms were used with three different seasonal wind speed climatologies: *Esbensen and Kushnir* [1981], wind scatterometer data from European Remote Sensing (ERS) Satellites, and winds derived from the Special Sensor Microwave/Imager (SSM/I). The *Esbensen and Kushnir* [1981] climatology was based on data from ships of opportunity and was selected for comparison with previous studies that used it. Sensitivity tests were also conducted with different SST and SSS climatologies. These included the World Ocean Atlas 1998 (WOA98) [*Conkright et al.*, 1998], the World Ocean Atlas 1994 (WOA94) [*Levitus and Boyer*, 1994], and the Reynolds and Smith SST [*Reynolds and Smith*, 1994] data. In order to simulate random error of SST and SSS fields, we mixed the WOA94 and WOA98 SST and SSS climatologies in our analyses.

### II.3 Sensitivity to Gas Transfer Algorithms and Wind Speed Climatologies

Results from the application of the three wind speed climatologies and four different gas transfer algorithms are provided for the global oceans and regional domains (Figure II-3)

in Table 1. Figure II-3 shows the spatial variability of the annual sea-air CO<sub>2</sub> flux for the four gas transfer algorithms and the SSM/I wind speed climatology. Figure II-4 shows the seasonal variability of sea-air CO<sub>2</sub> flux for the global oceans and for 6 regional oceanic domains derived from the four gas transfer algorithms and SSM/I winds. A summary of globally and regionally averaged wind speeds for the three wind data sets is provided in Table 2. The sea-air flux varies with the gas transfer algorithm and wind speed climatology used. The smallest global sea-air CO<sub>2</sub> flux (Table 1) is obtained with the *Liss and Merlivat* [1986] gas transfer algorithm for all three wind speed climatologies. The SSM/I winds produce the lowest global flux (-0.57 Gt/yr), while the ERS winds produce the highest flux (-0.70 Gt/yr). The winds from *Esbensen and Kushnir* [1981] yield a global sea-air flux (-0.65 Gt/yr) between those derived from the ERS and SSM/I winds. A negative sea-air flux represents uptake of CO<sub>2</sub> by the ocean. The largest global sea-air CO<sub>2</sub> flux is obtained with the *Wanninkhof and McGillis* [1999] gas transfer algorithm. This algorithm yields yearly global sea-air CO<sub>2</sub> fluxes of -1.73, -2.01, and -2.27 Gt/yr using the SSM/I, *Esbensen and Kushnir* [1981], and ERS wind climatologies, respectively. The Southern Ocean (-0.58 to -1.90 Gt/yr), North Atlantic (-0.27 to -0.73 Gt/yr), and North Pacific (-0.17 to -0.48 Gt/yr) are the largest sinks of CO<sub>2</sub> throughout the year. As shown in Figure II-4, the North Pacific becomes a weak source (0.02 to 0.13 Gt/yr) of CO<sub>2</sub> during the Boreal summer (July-August). The equatorial Pacific is the largest source of CO<sub>2</sub> (0.28 to 0.81 Gt/yr) with positive values throughout the year. The largest flux in the equatorial Pacific is obtained with the *Tans et al.* [1990] algorithm and SSM/I winds. The Indian Ocean and the equatorial Atlantic are weak sources of CO<sub>2</sub> throughout the year (0.04 to 0.16 Gt/yr).

As shown in Figure II-4, the Southern Ocean has the largest seasonal cycle with a peak in ocean uptake during January-February (-1.1 To 2.9 Gt/yr). The North Atlantic and North Pacific Oceans have a reduced seasonal cycle, with strongest uptake during fall-winter and nearly neutral conditions during the summer months. These regions have small outgassing (North Pacific) or small ingassing (North Atlantic) of CO<sub>2</sub> during the summer months because the potentially high *p*CO<sub>2</sub> values due to elevated SST conditions are counterbalanced by an increased *p*CO<sub>2</sub> drawdown by biological activity. The Indian Ocean, equatorial Pacific, and equatorial Atlantic have no distinctive seasonal cycle.

Our CO<sub>2</sub> flux estimates agree reasonably well with the estimates of *Takahashi et al.* [1997] using *Esbensen and Kushnir* [1981] winds. Their estimates using the *Liss and Merlivat* [1986], *Wanninkhof* [1992], and *Tans et al.* [1990] gas transfer algorithms are -0.71, -1.14, and -1.34 Gt/yr, respectively. Our equivalent estimates are -0.65, -1.28, and -1.22 Gt/yr. *Lefèvre et al.* [1999] compiled quarterly maps of  $\Delta p$ CO<sub>2</sub> interpolated from *p*CO<sub>2</sub> measurements in the North Atlantic and the North Pacific Oceans. Their estimates of the CO<sub>2</sub> flux for the Northern Hemisphere north of 10°N using SSM/I winds and the *Liss and Merlivat* [1986], *Wanninkhof* [1992], and *Tans et al.* [1990] algorithms are -0.45, -0.70, and -0.86 Gt/yr, respectively. Our equivalent estimates are -0.52, -1.02, and -1.08 Gt/yr. *Lefèvre et al.* [1999] estimates using *Esbensen and Kushnir* [1981] winds and the same three gas transfer algorithms are -0.37, -0.60, and -0.76 Gt/yr, respectively. Our equivalent estimates are -0.50, -0.98, -1.03 Gt/yr. Overall, our estimates are 15% to 35% higher than those of *Lefèvre et al.* [1999]. Since we used *p*CO<sub>2</sub> data based on

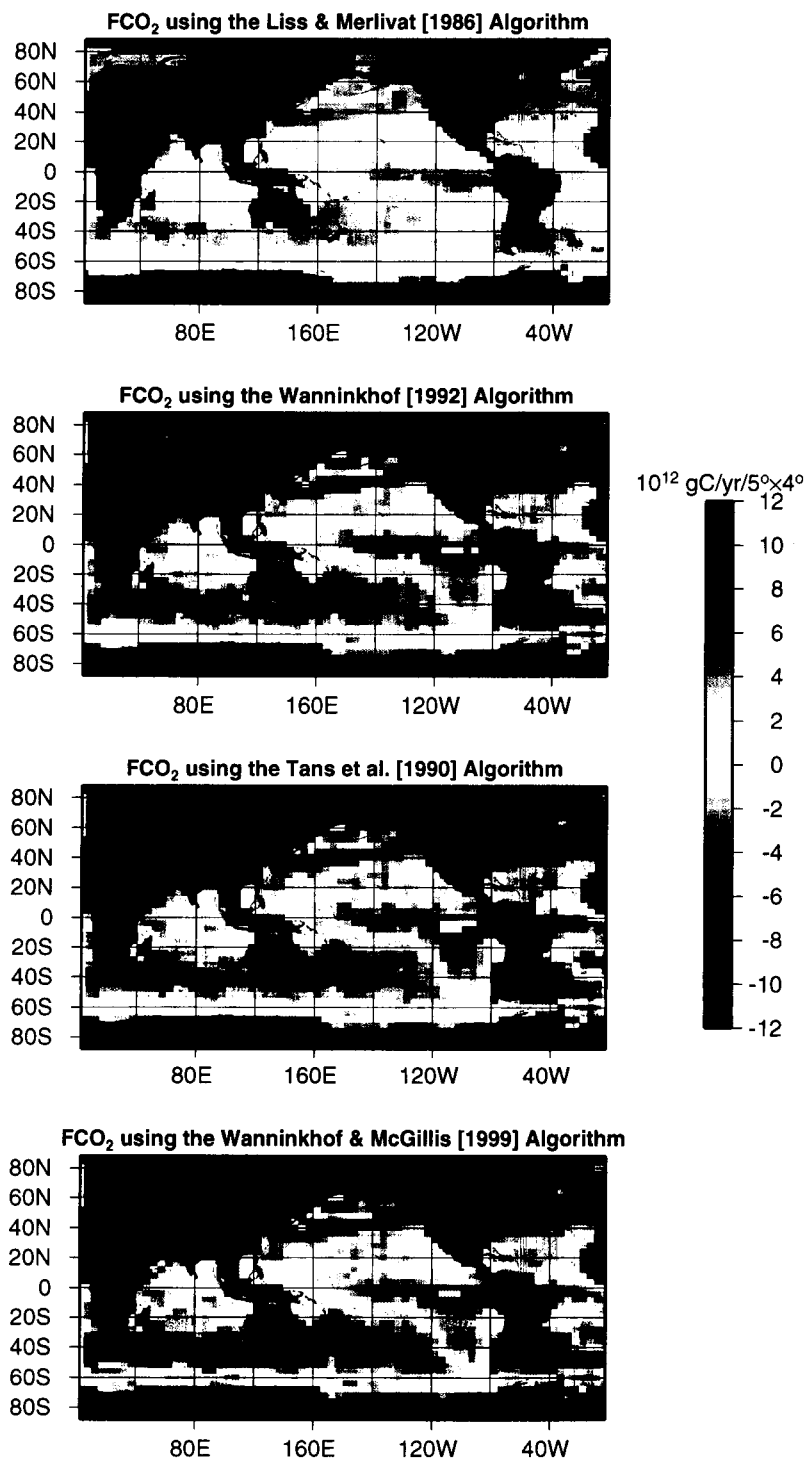


Figure II-3. Annual sea-air CO<sub>2</sub> flux for the global oceans derived from four different gas transfer algorithms and SSM/I seasonal wind climatologies.

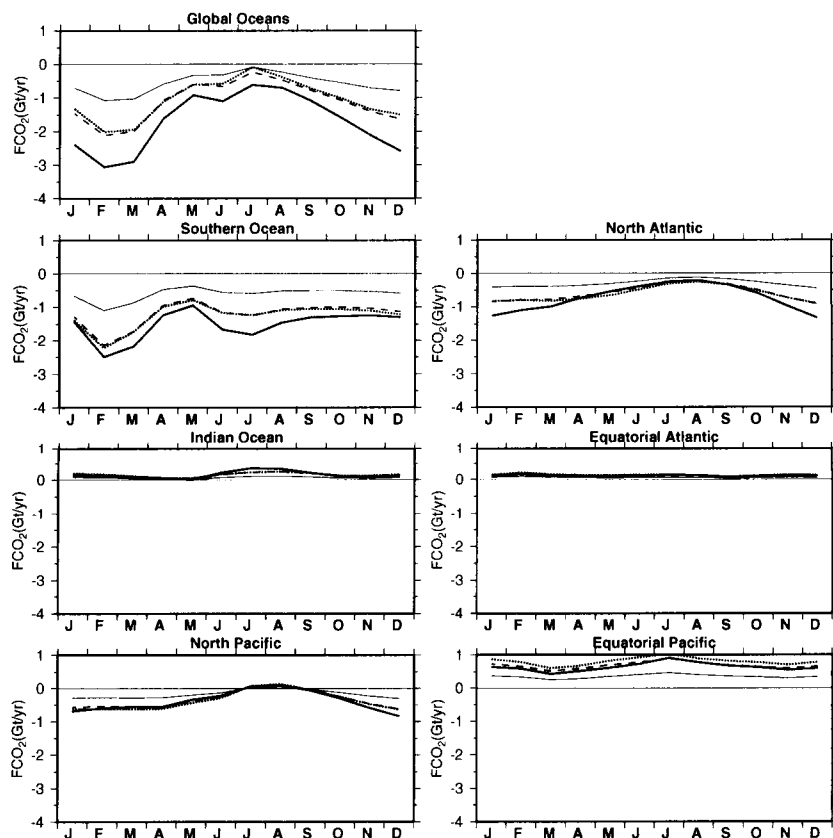


Figure II-4. Seasonal variability of sea-air CO<sub>2</sub> flux derived with SSM/I winds for the global oceans and xix different oceanic regions. The four separate lines, solid, dashed, dotted, and thick solid, represent the *Liss and Merlivat (1986)*, *Wanninkhof (1992)*, *Tans et al. (1990)*, and *Wanninkhof and McGillis (1999)* algorithms, respectively.

*Takahashi et al.* [1997], and *Lefèvre et al.* [1999] used revised  $p\text{CO}_2$  maps based on additional observations, we attribute our  $\text{CO}_2$  flux overestimates to the different  $p\text{CO}_2$  data sets used for the estimates.

## II.4 Sensitivity to SST and SSS Climatologies

Variability in SST and SSS global distributions affect the calculation of TA [Millero *et al.*, 1998],  $\text{TCO}_2$  [Lee *et al.*, 2000],  $\text{CO}_2$  solubility, the Schmidt number, and the ocean  $p\text{CO}_2$  via the dissociation constants for carbonic acid, boric acid, and sea water, which combine to affect the sea-air  $\text{CO}_2$  flux. The WOA98 SST and SSS data are used as a reference calculation to be compared with the results of other sea-air flux calculations using different combinations of SST and SSS climatologies. The *Tans et al.* [1990] gas transfer algorithm was used in all cases. The results are summarized in Table 3, which tabulates the  $\text{FCO}_2$  means and seasonal ranges, and the mean differences and standard deviations of SST, SSS, TA, and  $\text{TCO}_2$ . Globally, the mean ocean uptake of  $\text{CO}_2$  is 15.6% larger when the *Reynolds and Smith* [1994] SST data are used, and the seasonal range is 5.5% larger. The SST, TA, and  $\text{TCO}_2$  differences associated with the global sea-air flux change are  $-0.16 \pm 0.53$  °C,  $+0.26 \pm 1.61$   $\mu\text{mol kg}^{-1}$ , and  $+0.86 \pm 3.95$   $\mu\text{mol kg}^{-1}$ , respectively. The use of both SST and SSS from the WOA94 data causes an increase in ocean uptake of 4.6%, and a seasonal range increase of 5.1%. The combination of WOA98 SST and WOA94 SSS causes an increase of 6.4% in  $\text{CO}_2$  uptake, with a slight increase of seasonal range (1.4%). The global  $\text{CO}_2$  flux is least affected (-1.8%) when the combination of WOA98 SSS and WOA94 SST is used. The mean deviations in TA and  $\text{TCO}_2$  are also small in this case ( $-0.11 \pm 1.53$   $\mu\text{mol kg}^{-1}$  and  $-0.10 \pm 3.56$   $\mu\text{mol kg}^{-1}$ , respectively).

## II.5 Conclusions

Sensitivity analyses of sea-air  $\text{CO}_2$  flux to wind speed climatologies, gas transfer algorithms, SSS and SST were conducted for the global oceans and regional domains. Large uncertainties in the global sea-air flux are identified, primarily due to the different gas transfer algorithms used. However, two of the algorithms provide very close results. Globally, there is less than 9% difference between the *Tans et al.* [1990] and the *Wanninkhof* [1992] algorithms, which produce sea-air fluxes within the mid-range of our estimates. The use of three different wind climatologies with these two algorithms produces uncertainties of 7 to 10%. The other two algorithms [Liss and Merlivat, 1986; *Wanninkhof and McGillis*, 1999] differ by a factor of two and produce sea-air fluxes at the low end [Liss and Merlivat, 1986] and high end [*Wanninkhof and McGillis*, 1999] of our estimates. The sensitivity of the sea-air flux to SST and SSS is similar in magnitude to the effect of using different wind climatologies. Globally, the mean ocean uptake of  $\text{CO}_2$  changes by 5 to 16%, depending upon the combination of SST and SSS used.

## References

- Absoft, *Pro Fortran for Linux*, 154 pp., absoft, Rochester Hills, MI, 1997.
- AVISO, Validation and Interpretation of Satellite Data in Oceanography (AVISO) Handbook: Sea Level Anomaly Files, Publ. AVI-NT-001-312-CN, pp. 24, Cent. Natl. d'Etudes Spatiales, Toulouse, France, 1997.
- Baker, K.S., and R.C. Smith, Bio-Optical Classification and Model of Natural-Waters .2, *Limnology and Oceanography*, 27 (3), 500-509, 1982.
- Bates, N.R., A.H. Knap, F. Bahr, J. Benson, D.W. Chipman, F. Howse, R.J. Johnson, and T. Takahashi, Carbon dioxide measurements obtained aboard the R/V Weatherbird II in the Sargasso Sea, June-December 1994, January-December 1995, January-December 1996, Bermuda Biological Station For Research (BBSR) CO<sub>2</sub> Data Reports 98-1, 98-2, and 98-3, Ferry Reach, Bermuda, 1998.
- Bates, N.R., A.F. Michaels, and A.H. Knap, Seasonal and interannual variability of oceanic carbon dioxide species at the U.S. JGOFS Bermuda Atlantic Time-series Study (BATS) site, *Deep-Sea Res. II*, 43 (2-3), 347-383, 1996.
- Broecker, W.S., T.H. Peng, G. Ostlund, and M. Stuiver, The Distribution of Bomb Radiocarbon in the Ocean, *Journal of Geophysical Research-Oceans*, 90 (NC4), 6953-6970, 1985.
- Chen, F., and J.D. Annan, The influence of different turbulence schemes on modelling primary production in a 1D coupled physical-biological model, *Journal of Marine Systems*, 26 (3-4), 259-288, 2000.
- Christian, J.R., M.R. Lewis, and D.M. Karl, Vertical fluxes of carbon, nitrogen, and phosphorus in the North Pacific Subtropical Gyre near Hawaii, *Journal of Geophysical Research-Oceans*, 102 (C7), 15667-15677, 1997.
- Conkright, M., S. Levitus, T. O'Brien, T. Boyer, J. Antonov, and C. Stephens, World Ocean Atlas 1998 CD-ROM Data Set Documentation, *NODC Internal Report, Silver Spring, MD, Tech. Rep. 15*, 16 pp., 1998.
- Conway, T.J., and P.P. Tans, Atmospheric Carbon Dioxide Mixing Ratios from the NOAA Climate Monitoring and Diagnostics Laboratory Cooperative Flask Sampling Network, 1967-1993, pp. 202 pp., ORNL/CDIAC-73, NDP-005/R3. Carbon Dioxide Information Analysis, Oak Ridge National Laboratory, Oak Ridge, Tennessee, 1996.
- Dickson, A.G., and F.J. Millero, A Comparison of the Equilibrium-Constants for the Dissociation of Carbonic-Acid in Seawater Media, *Deep-Sea Research Part a-Oceanographic Research Papers*, 34 (10), 1733-1743, 1987.
- Dupouy, C., J. Neveux, and J.M. Andre, Spectral absorption coefficient of photosynthetically active pigments in the equatorial Pacific Ocean (165 degrees E-150 degrees W), *Deep-Sea Research Part II-Topical Studies in Oceanography*, 44 (9-10), 1881-1906, 1997.
- Esbensen, S.K., and V. Kushnir, The heat budget of the global ocean: An atlas based on estimates from surface marine observations. Tech. Rep. 29, Clim. Res. Inst., Oreg. State Univ., Corvallis, 1981.
- Fennel, K., Y.H. Spitz, R.M. Letelier, M.R. Abbott, and D.M. Karl, A deterministic model for N-2 fixation at stn. ALOHA in the subtropical North Pacific Ocean, *Deep-Sea Research Part II-Topical Studies in Oceanography*, 49 (1-3), 149-174, 2002.
- Frouin, R., D.W. Lingner, C. Gautier, K.S. Baker, and R.C. Smith, A Simple Analytical Formula to Compute Clear Sky Total and Photosynthetically Available Solar Irradiance at the Ocean Surface, *Journal of Geophysical Research-Oceans*, 94 (C7), 9731-9742, 1989.
- Gabric, A.J., G.P. Ayers, and G.C. Sander, Independent marine and atmospheric model estimates of the sea- air flux of dimethylsulfide in the Southern Ocean, *Geophysical Research Letters*, 22 (24), 3521-3524, 1995.
- Garver, S.A., and D.A. Siegel, Inherent optical property inversion of ocean color spectra and its biogeochemical interpretation .1. Time series from the Sargasso Sea, *Journal of Geophysical Research-Oceans*, 102 (C8), 18607-18625, 1997.
- Garwood, R.W., An oceanic mixed-layer model capable of simulating cyclic states, *J. Phys. Oceanogr.*, 7, 455-471, 1977.
- Gregg, W.W., and K.L. Carder, A Simple Spectral Solar Irradiance Model for Cloudless Maritime Atmospheres, *Limnology and Oceanography*, 35 (8), 1657-1675, 1990.
- Kalnay, E., M. Kanamitsu, R. Kistler, W. Collins, D. Deaven, L. Gandin, M. Iredell, S. Saha, G. White, J. Woollen, Y. Zhu, M. Chelliah, W. Ebisuzaki, W. Higgins, J. Janowiak, K.C. Mo, C. Ropelewski,

- J. Wang, A. Leetmaa, R. Reynolds, R. Jenne, and D. Joseph, The NCEP/NCAR 40-year reanalysis project, *Bulletin of the American Meteorological Society*, 77 (3), 437-471, 1996.
- Keeling, R.F., B.B. Stephens, R.G. Najjar, S.C. Doney, D. Archer, and M. Heimann, Seasonal variations in the atmospheric O<sub>2</sub>/N<sub>2</sub> ratio in relation to the kinetics of air-sea gas exchange, *Global Biogeochemical Cycles*, 12 (1), 141-163, 1998.
- Lee, K., F.J. Millero, and R. Wanninkhof, The carbon dioxide system in the Atlantic Ocean, *Journal of Geophysical Research-Oceans*, 102 (C7), 15693-15707, 1997.
- Lee, K., R. Wanninkhof, R.A. Feely, F.J. Millero, and T.H. Peng, Global relationships of total inorganic carbon with temperature and nitrate in surface seawater, *Global Biogeochemical Cycles*, 14 (3), 979-994, 2000.
- Lefèvre, N., A.J. Watson, D.J. Cooper, R.F. Weiss, T. Takahashi, and S.C. Sutherland, Assessing the seasonality of the oceanic sink for CO<sub>2</sub> in the northern hemisphere, *Global Biogeochemical Cycles*, 13 (2), 273-286, 1999.
- Levitus, S., and T. Boyer, World Ocean Atlas 1994 Vol. 4: Temperature. NOAA Atlas NESDIS 4, pp. 117, U.S. Department of Commerce, Washington, D.C., 1994.
- Liss, P.S., and L. Merlivat, Air-sea gas exchange rates: Introduction and synthesis, in *The Role of Air-Sea Exchange in Geochemical Cycling*, edited by P. Buat-Ménard, pp. 113-129, D. Reidel, Hingham, Mass., 1986.
- McClain, C.R., K. Arrigo, K.S. Tai, and D. Turk, Observations and simulations of physical and biological processes at ocean weather station P, 1951-1980, *J. Geophys. Res.*, 101 (C2), 3697-3713, 1996.
- McGillicuddy, D.J., R. Johnson, D.A. Siegel, A.F. Michaels, N.R. Bates, and A.H. Knap, Mesoscale variations of biogeochemical properties in the Sargasso Sea, *Journal of Geophysical Research-Oceans*, 104 (C6), 13381-13394, 1999.
- McGillicuddy, D.J., A.R. Robinson, D.A. Siegel, H.W. Jannasch, R. Johnson, T.D. Dickey, J. McNeil, A.F. Michaels, and A.H. Knap, Influence of mesoscale eddies on new production in the Sargasso Sea, *Nature*, 394, 263-265, 1998a.
- McGillicuddy, D.J., A.R. Robinson, D.A. Siegel, H.W. Jannasch, R. Johnson, T. Dickey, J. McNeil, A.F. Michaels, and A.H. Knap, Influence of mesoscale eddies on new production in the Sargasso Sea, *Nature*, 394 (6690), 263-266, 1998b.
- McGillis, W.R., J.B. Edson, J.E. Hare, and C.W. Fairall, Direct covariance air-sea CO<sub>2</sub> fluxes, *Journal of Geophysical Research-Oceans*, 106 (C8), 16729-16745, 2001.
- Mellor, G.L., Analytic Prediction of Properties of Stratified Planetary Surface-Layers, *Journal of the Atmospheric Sciences*, 30 (6), 1061-1069, 1973.
- Mellor, G.L., and T. Yamada, Development of a turbulence closure model for geophysical fluid problems, *Rev. Geophys. and Space Phys.*, 20, 851-875, 1982.
- Michaels, A.F., and A.H. Knap, Overview of the U.S. JGOFS Bermuda Atlantic Time-series Study and Hydrostation S program, *Deep-Sea Res. II*, 43, 157-198, 1996.
- Michaels, A.F., A.H. Knap, R.L. Dow, K. Gundersen, R.J. Johnson, J. Sorensen, A. Close, G.A. Knauer, S.E. Lohrenz, V.A. Asper, M. Tuel, and R. Bidigare, Seasonal Patterns of Ocean Biogeochemistry at the United-States JGOFS Bermuda Atlantic Time-Series Study Site, *Deep-Sea Research Part I-Oceanographic Research Papers*, 41 (7), 1013-1038, 1994.
- Millero, F.J., K. Lee, and M. Roche, Distribution of alkalinity in the surface waters of the major oceans, *Marine Chemistry*, 60 (1-2), 111-130, 1998.
- Morel, A., Optical Modeling of the Upper Ocean in Relation to Its Biogenous Matter Content (Case-I Waters), *Journal of Geophysical Research-Oceans*, 93 (C9), 10749-10768, 1988.
- Moum, J.N., and T.R. Osborn, Mixing in the Main Thermocline, *Journal of Physical Oceanography*, 16 (7), 1250-1259, 1986.
- Neumann, G., and W.J. Pierson, *Principles of Physical Oceanography*, 545 pp., Prentice-Hall, Inc., Englewood Cliffs, N.J., 1966.
- Nightingale, P.D., G. Malin, C.S. Law, A.J. Watson, P.S. Liss, M.I. Liddicoat, J. Boutin, and R.C. Upstill-Goddard, In situ evaluation of air-sea gas exchange parameterizations using novel conservative and volatile tracers, *Global Biogeochemical Cycles*, 14 (1), 373-387, 2000.
- Oberhuber, J.M., An Atlas Based on the COADS Data Set: The Budgets of Heat, Buoyancy and Turbulent Kinetic Energy at the Surface of the Global Ocean, pp. 20, Max-Planck-Institut für Meteorologie, Hamburg, 1988.

- Oschlies, A., Can eddies make ocean deserts bloom?, *Global Biogeochem. Cycles*, 16 (4), 1106, doi:10.1029/2001GB001830, 2002.
- Pope, R.M., and E.S. Fry, Absorption spectrum (380-700 nm) of pure water .2. Integrating cavity measurements, *Applied Optics*, 36 (33), 8710-8723, 1997.
- Reynolds, R.W., and T.M. Smith, Improved Global Sea-Surface Temperature Analyses Using Optimum Interpolation, *Journal of Climate*, 7 (6), 929-948, 1994.
- Richtmyer, R.D., and K.W. Morton, *Difference Methods for Initial-Value Problems*, 405 pp., Interscience, 1967.
- Sharples, J., C.M. Moore, and E.R. Abraham, Internal tide dissipation, mixing, and vertical nitrate flux at the shelf edge of NE New Zealand, *Journal of Geophysical Research-Oceans*, 106 (C7), 14069-14081, 2001.
- Siegel, D.A., and J.A. Domaradzki, Large-Eddy Simulation of Decaying Stably Stratified Turbulence, *Journal of Physical Oceanography*, 24 (11), 2353-2386, 1994.
- Siegel, D.A., D.J. McGillicuddy, and E.A. Fields, Mesoscale eddies, satellite altimetry, and new production in the Sargasso Sea, *Journal of Geophysical Research-Oceans*, 104 (C6), 13359-13379, 1999.
- Siegel, D.A., A.F. Michaels, J.C. Sorensen, M.C. Obrien, and M.A. Hammer, Seasonal Variability of Light Availability and Utilization in the Sargasso Sea, *Journal of Geophysical Research-Oceans*, 100 (C5), 8695-8713, 1995.
- Signorini, S.R., and C.R. McClain, Sensitivity of Global Sea-Air CO<sub>2</sub> Flux to Gas Transfer Algorithms, Climatological Wind Speeds, and Variability of Sea Surface Temperature and Salinity, pp. 25, NASA Goddard Space Flight Center, Greenbelt, 2002.
- Signorini, S.R., C.R. McClain, and J.R. Christian, Modeling biogeochemical-physical interactions and carbon flux in the Sargasso Sea (Bermuda Atlantic Time-series Study site), in *NASA/TP 209991*, pp. 37, NASA Goddard Space Flight Center, Greenbelt, MD, 2001a.
- Signorini, S.R., C.R. McClain, J.R. Christian, and C.S. Wong, Seasonal and interannual variability of phytoplankton, nutrients, TCO<sub>2</sub>, pCO<sub>2</sub>, and O<sub>2</sub> in the eastern Subarctic Pacific, *J. Geophys. Res.*, 106 (C12), 31,197-31,215, 2001b.
- Simpson, J.J., and T.D. Dickey, The Relationship between Downward Irradiance and Upper Ocean Structure, *Journal of Physical Oceanography*, 11 (3), 309-323, 1981.
- Smethie, W.M., T. Takahashi, and D.W. Chipman, Gas-Exchange and Co<sub>2</sub> Flux in the Tropical Atlantic-Ocean Determined from Rn-222 and Pco<sub>2</sub> Measurements, *Journal of Geophysical Research-Oceans*, 90 (NC4), 7005-7022, 1985.
- Takahashi, T., R.A. Feely, R.F. Weiss, R.H. Wanninkhof, D.W. Chipman, S.C. Sutherland, and T.T. Takahashi, Global air-sea flux of CO<sub>2</sub>: An estimate based on measurements of sea-air pCO<sub>2</sub> difference, *Proceedings of the National Academy of Sciences of the United States of America*, 94 (16), 8292-8299, 1997.
- Tans, P.P., I.Y. Fung, and T. Takahashi, Observational Constraints on the Global Atmospheric CO<sub>2</sub> Budget, *Science*, 247 (4949), 1431-1438, 1990.
- Wanninkhof, R., Relationship between Wind-Speed and Gas-Exchange over the Ocean, *Journal of Geophysical Research-Oceans*, 97 (C5), 7373-7382, 1992.
- Wanninkhof, R., and W.R. McGillis, A cubic relationship between air-sea CO<sub>2</sub> exchange and wind speed, *Geophysical Research Letters*, 26 (13), 1889-1892, 1999.



REPORT DOCUMENTATION PAGE			Form Approved OMB No. 0704-0188	
Public reporting burden for this collection of information is estimated to average 1 hour per response, including the time for reviewing instructions, searching existing data sources, gathering and maintaining the data needed, and completing and reviewing the collection of information. Send comments regarding this burden estimate or any other aspect of this collection of information, including suggestions for reducing this burden, to Washington Headquarters Services, Directorate for Information Operations and Reports, 1215 Jefferson Davis Highway, Suite 1204, Arlington, VA 22202-4302, and to the Office of Management and Budget, Paperwork Reduction Project (0704-0188), Washington, DC 20503.				
1. AGENCY USE ONLY (Leave blank)		2. REPORT DATE July 2003	3. REPORT TYPE AND DATES COVERED Technical Memorandum	
4. TITLE AND SUBTITLE  Further Studies on Oceanic Biogeochemistry and Carbon Cycling			5. FUNDING NUMBERS  Code 970	
6. AUTHOR(S) S.R. Signorini, C.R. McClain				
7. PERFORMING ORGANIZATION NAME(S) AND ADDRESS (ES)  Goddard Space Flight Center Greenbelt, Maryland 20771			8. PERFORMING ORGANIZATION REPORT NUMBER 2003-02527-0	
9. SPONSORING / MONITORING AGENCY NAME(S) AND ADDRESS (ES)  National Aeronautics and Space Administration Washington, DC 20546-0001			10. SPONSORING / MONITORING AGENCY REPORT NUMBER TM-2003-212245	
11. SUPPLEMENTARY NOTES  S.R. Signorini, SAIC, Beltsville, MD				
12a. DISTRIBUTION / AVAILABILITY STATEMENT Unclassified-Unlimited Subject Category: 48 Report available from the NASA Center for AeroSpace Information, 7121 Standard Drive, Hanover, MD 21076-1320. (301) 621-0390.			12b. DISTRIBUTION CODE	
13. ABSTRACT (Maximum 200 words) This TM consists of two chapters. Chapter I describes the development of a coupled, one-dimensional biogeochemical model using turbulence closure mixed layer (TCMLM) dynamics. The model is applied to the Sargasso Sea at the BATS (Bermuda Atlantic Time Series) site and the results are compared with a previous model study in the same region described in NASA/TP-2001-209991. The use of the TCMLM contributed to some improvements in the model simulation of chlorophyll, PAR, nitrate, phosphate, and oxygen, but most importantly, the current model achieved good agreement with the data with much more realistic background eddy diffusivity. However, off-line calculations of horizontal transport of biogeochemical properties revealed that one-dimensional dynamics can only provide a limited assessment of the nutrient and carbon balances at BATS. Future studies in the BATS region will require comprehensive three-dimensional field studies, combined with three-dimensional eddy resolving numerical experiments, to adequately quantify the impact of the local and remote forcing on ecosystem dynamics and carbon cycling.  Chapter II addresses the sensitivity of global sea-air CO <sub>2</sub> flux estimates to wind speed, temperature, and salinity. Sensitivity analyses of sea-air CO <sub>2</sub> flux to wind speed climatologies, gas transfer algorithms, SSS and SST were conducted for the global oceans and regional domains. Large uncertainties in the global sea-air flux are identified, primarily due to the different gas transfer algorithms used. The sensitivity of the sea-air flux to SST and SSS is similar in magnitude to the effect of using different wind climatologies. Globally, the mean ocean uptake of CO <sub>2</sub> changes by 5 to 16%, depending upon the combination of SST and SSS used.				
14. SUBJECT TERMS biogeochemistry, carbon cycling			15. NUMBER OF PAGES 57	
			16. PRICE CODE	
17. SECURITY CLASSIFICATION OF REPORT Unclassified	18. SECURITY CLASSIFICATION OF THIS PAGE Unclassified	19. SECURITY CLASSIFICATION OF ABSTRACT Unclassified	20. LIMITATION OF ABSTRACT UL	